Interlayer hybridization in graphene quasicrystal and other bilayer graphene systems

Guodong Yu [1,3], Yunhua Wang,[2,4,*] Mikhail I. Katsnelson,[4] Hai-Qing Lin,[2] and Shengjun Yuan [3,2,4,†]

[1]*Center for Quantum Sciences and School of Physics, Northeast Normal University, Changchun 130024, China*
[2]*Beijing Computational Science Research Center, Beijing 100193, China*
[3]*Key Laboratory of Artificial Micro- and Nano-structures of Ministry of Education and School of Physics and Technology,*
Wuhan University, Wuhan 430072, China
[4]*Institute for Molecules and Materials, Radboud University, Heijendaalseweg 135, NL-6525 AJ Nijmegen, Netherlands*

The incommensurate $30°$ twisted bilayer graphene (BG) possesses both relativistic Dirac fermions and quasiperiodicity with 12-fold rotational symmetry arising from the interlayer interaction [Ahn *et al.*, Science **361**, 782 (2018) and Yao *et al.*, Proc. Natl. Acad. Sci. USA **115**, 6928 (2018)]. Understanding how the interlayer states interact with each other is of vital importance for identifying and subsequently engineering the quasicrystalline order in the layered structure. Herein, via symmetry and group representation theory we unravel the interlayer hybridization selection rules governing the interlayer coupling in both untwisted and twisted BG systems. Compared with the only allowed equivalent hybridization in D_{6h} untwisted BG, D_6 twisted BG permits equivalent and mixed hybridizations, and D_{6d} graphene quasicrystal allows both equivalent and nonequivalent hybridizations. The energy-dependent hybridization strengths in graphene quasicrystal and D_6 twisted BG show two remarkable characteristics: (i) near the Fermi level the weak hybridization owing to the relatively large energy difference between Dirac bands from top and bottom layers, and (ii) in high-energy regions the electron-hole asymmetry of hybridization strength with stronger interlayer coupling for holes, which arises from the non-nearest-neighbor interlayer hoppings and the wave-function phase difference between pairing states. These hybridization-generated band structures and their hybridization strength characteristics are verified by the calculated optical conductivity spectra. Our theoretical study paves a way for revealing the interlayer hybridization in van der Waals layered systems.

I. INTRODUCTION

Aside from the emergent correlated effects [1–16] in slightly twisted bilayer graphene (BG), the recently discovered quasicrystal [17,18] in $30°$ incommensurately twisted BG has also attracted considerable interests in both experiment [17–25] and theory [26–34]. Several synthetic methods have been used to successfully grow graphene quasicrystal on various substrates [17–20,23–25]. The quasiperiodicity in these samples is experimentally identified by the low-energy electron diffraction [17–20], transmission electron microscopy [17,24], scanning tunneling microscopy [21], Raman spectroscopy [18,23], and magnetotransport measurements [21,23]. The angle-resolved photoemission spectroscopy measurements (ARPES) indicate the multiple Dirac cones together with 12-fold rotational symmetry [17,18]. Owing to the interlayer scatterings with a constraint of the generalized umklapp scatterings, replica Dirac cone bands display unbalanced electron distribution features in ARPES [22]. In theoretical aspects, a **k**-space tight-binding model is constructed to explore the 12-fold symmetric resonant states and the critical characteristic of wave functions as a hallmark of quasicrystalline order is also verified [27]. The quantum

oscillations with spiral Fermi surfaces are predicted theoretically due to the quasiperiodicity and weak interlayer coupling [30]. Numerical simulations indicate that a fractal feature happens for the sliding force and the low friction appears as a result of the quasicrystalline structure [28]. The vertical pressure, electric field, and double stacking can be utilized to tune or remain the quasicrystalline electronic states [32,33]. In doped graphene quasicrystal, a combination of high symmetry and Coulomb interaction possibly enables another topological superconductivity [35]. All of these peculiar physical properties make graphene quasicrystal quite distinctive from graphene monolayer.

Compared with the conventional quasicrystals where all of the atoms are intrinsically located within a quasiperiodic order [36,37], graphene quasicrystal is viewed as an extrinsic quasicrystal (i.e., engineered quasicrystals) because its quasiperiodicity arises from the interlayer coupling between two graphene monolayers. Thus, *figuring out the origin of quasicrystalline order requires a deep understanding of how the interlayer states interact with each other*. The interlayer hybridization is defined that two pairing states belonging to different layers are hybridized with each other to generate the hybridization states (i.e., bonding and antibonding states), which are the eigenstates of the bilayer system. The interlayer hybridization matrix element is defined as $U_{ir,ir'} = \langle \varphi_{ir}^b | U | \varphi_{ir'}^t \rangle$, where φ_{ir}^b and $\varphi_{ir'}^t$ are the states of the bottom and top layers with irreducible representations (irreps) ir and ir',
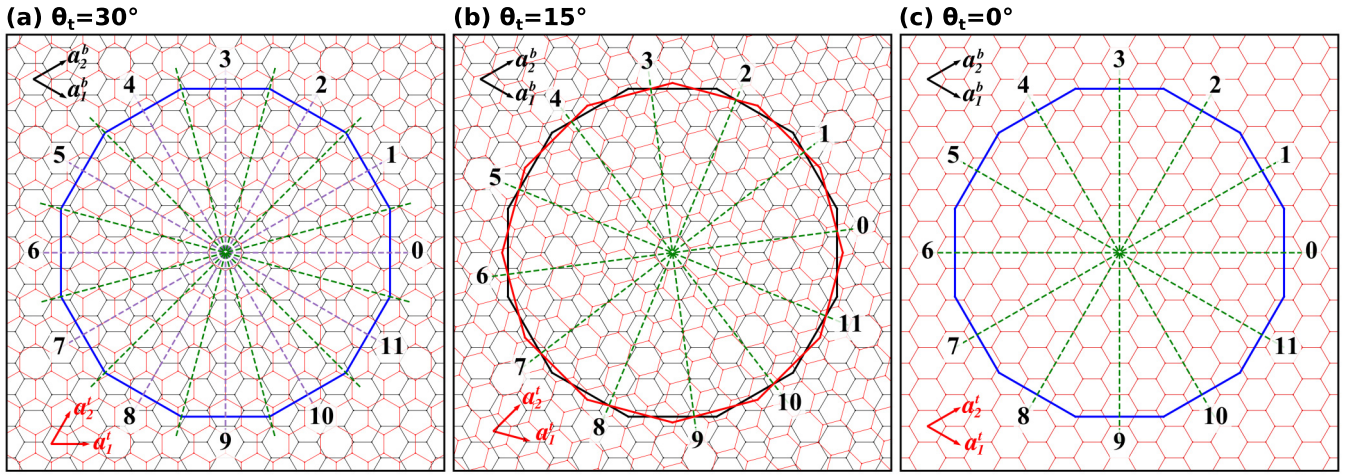
*wangyunhua@csrc.ac.cn
†s.yuan@whu.edu.cn

FIG. 1. Top view of structures of twisted BGs and their quantum dots for (a) $\theta_t = 30°$, (b) $\theta_t = 15°$, and (c) $\theta_t = 0°$. In (a), the edges of the D_{6d} quantum dot are denoted by the bottom and top blue lines, six σ_d reflection planes, and six twofold rotational axes are represented, respectively, by the dashed purple and green lines, and for each C_{6v} monolayer the vertical planes denoted by the lines (0–6, 2–8, 4–10) and the lines (1–7, 3–9, 5–11) are the reflection planes of three σ_v and three σ_d operations. In (b), the edges of the D_6 quantum dot are denoted by the bottom black thick lines and the top red thick lines, and the lines (0–6, 2–8, 4–10) and the lines (1–7, 3–9, 5–11) stand for the twofold axes of three C_2' and three C_2'' rotations, respectively. In (c) the edges of the D_{6h} quantum dot are denoted by the bottom and top blue lines, the vertical planes denoted by the lines (0–6, 2–8, 4–10) and the lines (1–7, 3–9, 5–11) are the reflection planes of three σ_v and three σ_d, and the lines (0–6, 2–8, 4–10) and the lines (1–7, 3–9, 5–11) also stand for the twofold axes of three C_2' and three C_2'' rotations, respectively. Here, each monolayer of quantum dots has the C_{6v} symmetry, and the sizes for the three different quantum dot structures are the size 6 (see the definition for the size of quantum dots in Sec. II).

respectively, and U is the interlayer coupling. The nonzero $U_{ir,ir'}$ means that the two states φ_{ir}^b and $\varphi_{ir'}^t$ can be the pairing states for interlayer hybridizations.

In this paper, we construct the interlayer hybridization selection rules (in Table V) governing which states from two layers are allowed to be hybridized in D_{6h} untwisted BG, D_6 twisted BG, and D_{6d} graphene quasicrystal. We find that the allowed hybridizations include (i) equivalent hybridization, for which the irreps for pairing states are the same, in all BG systems, (ii) mixed hybridization, for which the pairing states can have both the same and different irreps, in D_6 twisted BG, and (iii) nonequivalent hybridization, for which the irreps of the pairing states are different, in graphene quasicrystal. Our numerical calculations of the interlayer hybridization matrix elements from p_z orbital tight-binding (TB) model, Wannier-orbital TB model, and density functional theory (DFT) calculations further verify the interlayer hybridization selection rules. The calculated energy-dependent hybridization strengths show that (i) the interlayer hybridization inside low-energy areas is weak in twisted BG because of a relatively large energy difference between the Dirac bands from top and bottom layers, and (ii) inside the high-energy areas an electron-hole asymmetry of hybridization strength exists as a result of non-nearest-neighbor interlayer hoppings and the wave-function phase difference of the pairing states. The obtained optical conductivity spectra with remarkably different absorption features at different chemical potentials further manifest the hybridization strength characteristics and hybridization-induced band structures in graphene quasicrystals.

The rest of this paper is organized as follows. In Sec. II, the structures of graphene quasicrystal, twisted BG, and untwisted BG are presented. In Secs. III and IV, we discuss,

respectively, the interlayer hybridization selection rules and the hybridization classification, which are further verified by using p_z-orbital TB, Wannier-orbital TB, and DFT calculations in Sec. V. In Sec. VI, we introduce the energy-dependent interlayer hybridization strength. We further discuss the weak hybridization around the Fermi level, the electron-hole asymmetrical hybridizations inside high-energy areas, and the electric field effects on hybridization strengths and resonant quasicrystalline states. In Sec. VII, we present proposals for identifying the hybridization-generated band structures of graphene quasicrystal. In Sec. VIII, we summarize our main conclusions.

II. STRUCTURES

Figure 1(a) shows the structure and symmetry operations of graphene quasicrystal (30° twisted BG). The lattice vectors for bottom and top graphene monolayers are $\boldsymbol{a}_1^b = \frac{\sqrt{3}a}{2}\boldsymbol{i} - \frac{a}{2}\boldsymbol{j}$, $\boldsymbol{a}_2^b = \frac{\sqrt{3}a}{2}\boldsymbol{i} + \frac{a}{2}\boldsymbol{j}$ and $\boldsymbol{a}_1^t = a\boldsymbol{i} + 0\boldsymbol{j}$, $\boldsymbol{a}_2^t = \frac{a}{2}\boldsymbol{i} + \frac{\sqrt{3}a}{2}\boldsymbol{j}$, respectively, where $a = 2.46$ Å is the lattice constant of graphene, and $h = 3.35$ Å is the interlayer distance. The relative positions of the sublattices in a unit cell for bottom and top graphene monolayers are $\boldsymbol{\tau}_A^b = \frac{1}{3}\boldsymbol{a}_1^b + \frac{1}{3}\boldsymbol{a}_2^b$, $\boldsymbol{\tau}_B^b = \frac{2}{3}\boldsymbol{a}_1^b + \frac{2}{3}\boldsymbol{a}_2^b$ and $\boldsymbol{\tau}_A^t = \frac{1}{3}\boldsymbol{a}_1^t + \frac{1}{3}\boldsymbol{a}_2^t$, $\boldsymbol{\tau}_B^t = \frac{2}{3}\boldsymbol{a}_1^t + \frac{2}{3}\boldsymbol{a}_2^t$, respectively. The rotation center is located at the hexagon center of both two layers. The graphene quasicrystal has D_{6d} symmetry, and the graphene monolayers have C_{6v} symmetry. The character tables of C_{6v} and D_{6d} are listed in Tables I and II, respectively. A twisted BG with $0° < \theta_t < 30°$ is obtained by rotating the top layer of graphene quasicrystal with a angle of $30° - \theta_t$ clockwise, as shown in Fig. 1(b), where a twisted BG with $\theta_t = 15°$ as an example is generated. The twisted BG with

TABLE I. Character table of C_{6v}.

C_{6v}	E	$2C_6$	$2C_3$	C_2	$3\sigma_v$	$3\sigma_d$
A_1	1	1	1	1	1	1
A_2	1	1	1	1	−1	−1
B_1	1	−1	1	−1	1	−1
B_2	1	−1	1	−1	−1	1
E_1	2	1	−1	−2	0	0
E_2	2	−1	−1	2	0	0

TABLE III. Character tables of D_6.

D_6	E	$2C_6$	$2C_3$	C_2	$3C_2'$	$3C_2''$
A_1	1	1	1	1	1	1
A_2	1	1	1	1	−1	−1
B_1	1	−1	1	−1	1	−1
B_2	1	−1	1	−1	−1	1
E_1	2	1	−1	−2	0	0
E_2	2	−1	−1	2	0	0

$0° < \theta_t < 30°$ has D_6 symmetry. The character table of D_6 is listed in Table III. The untwisted BG is the AA-stacked BG with $\theta_t = 0°$ and D_{6h} symmetry. Figure 1(c) shows the structure and symmetry operations of the untwisted BG. The character table of D_{6h} is listed in Table IV. In Figs. 1(a)–1(c), twisted BG quantum dots with the same point-group symmetries as their bulks in the corresponding three systems are also sketched. The quantum dot structures consist of the bottom and top dodecagons with their edges labeled by the corresponding numbers from 0 to 11. The size of the quantum dot is measured by the number n of zigzag chains from the rotation center to an arbitrary edge of the quantum dot structure, and the size is thus labeled by size n. In Figs. 1(a)–1(c), the sizes for the three quantum dots are the size 6.

III. HYBRIDIZATION SELECTION RULES

For an arbitrary twisted BG consisting of two C_{6v} monolayers with a twist angle θ_t, the Hamiltonian includes three terms,

$$H = H_0^b + H_0^t + U, \tag{1}$$

where H_0^b and H_0^t are the Hamiltonians of the bottom and top layers with the corresponding layer indices b and t, respectively, and U is the interlayer coupling. Because of the θ_t-dependent symmetry properties, the twisted BG structures are divided into D_{6h} ($\theta_t = 0°$), D_6 ($0° < \theta_t < 30°$), and D_{6d} ($\theta_t = 30°$) point groups, as listed in Table V. The Hamiltonians and reflection operations of the bottom and top layers are connected by the rotation operation $R(\theta_t)$ and the mirror reflection σ_h with its mirror plane perpendicular to the z axis. Therefore, we can write the Hamiltonian H_0^t of the top layer as

$$H_0^t = [\sigma_h R(\theta_t)]H_0^b[\sigma_h R(\theta_t)]^\dagger, \tag{2}$$

and the reflection operations between the top and bottom layers as

$$\sigma_{v,i}^t = R(\theta_t)\sigma_{v,i}^b[R(\theta_t)]^\dagger,$$
$$\sigma_{d,i}^t = R(\theta_t)\sigma_{d,i}^b[R(\theta_t)]^\dagger, \tag{3}$$
$$\sigma_{d,i}^{b/t} = R(\pi/6)\sigma_{v,i}^{b/t}[R(\pi/6)]^\dagger,$$

where $i = 0, 1, 2$, and $\sigma_{v,0}^b = \sigma_x$. We note that the C_{6v} point groups of the two layers are different due to the twist, namely, $C_{6v}^b \neq C_{6v}^t$. The character projection operator of the irrep ir for a point group α is defined as

$$P_{ir}^\alpha = \frac{l_{ir}}{g} \sum_{R \in \alpha} \chi_{ir}^*(R)O_R, \tag{4}$$

where l_{ir} and g are the dimension of irrep ir and the order of α, respectively, and $\chi_{ir}(R)$ is the character of matrix representation O_R of the symmetry operation R for irrep ir. The projection operator can be used to determine which irrep a state has according to

$$P_{ir}^\alpha|\varphi_{ir'}\rangle = \delta_{ir,ir'}|\varphi_{ir'}\rangle. \tag{5}$$

Due to Eq. (2), the state of the bottom layer $|\varphi_{ir}^b\rangle$ and the state of the top layer $|\varphi_{ir'}^t\rangle = [\sigma_h R(\theta_t)]|\varphi_{ir}^b\rangle$ always have the same irreps (i.e., $ir' = ir$) and the same energy. Using the projection operator in Eqs. (4) and (5) and performing some algebraic calculations (see Appendixes A and B), we obtain the constraint equations of the hybridization matrix element $U_{ir,ir'} = \langle\varphi_{ir}^b|U|\varphi_{ir'}^t\rangle$ for all three BG systems, where $|\varphi_{ir}^b\rangle$ and $|\varphi_{ir'}^t\rangle$ are the states of the bottom and top layers with irreps ir and ir', respectively. These constraint

TABLE IV. Character table of D_{6h}.

D_{6h}	E	$2C_6$	$2C_3$	C_2	$3C_2'$	$3C_2''$	i	$2S_3$	$2S_6$	σ_h	$3\sigma_d$	$3\sigma_v$
A_{1g}	1	1	1	1	1	1	1	1	1	1	1	1
A_{2g}	1	1	1	1	−1	−1	1	1	1	1	−1	−1
B_{1g}	1	−1	1	−1	1	−1	1	−1	1	−1	1	−1
B_{2g}	1	−1	1	−1	−1	1	1	−1	1	−1	−1	1
E_{1g}	2	1	−1	−2	0	0	2	1	−1	−2	0	0
E_{2g}	2	−1	−1	2	0	0	2	−1	−1	2	0	0
A_{1u}	1	1	1	1	1	1	−1	−1	−1	−1	−1	−1
A_{2u}	1	1	1	1	−1	−1	−1	−1	−1	−1	1	1
B_{1u}	1	−1	1	−1	1	−1	−1	1	−1	1	−1	1
B_{2u}	1	−1	1	−1	−1	1	−1	1	−1	1	1	−1
E_{1u}	2	1	−1	−2	0	0	−2	−1	1	2	0	0
E_{2u}	2	−1	−1	2	0	0	−2	1	1	−2	0	0

TABLE II. Character table of D_{6d}.

D_{6d}	E	$2S_{12}$	$2C_6$	$2S_4$	$2C_3$	$2S_{12}^5$	C_2	$6C_2'$	$6\sigma_d$
A_1	1	1	1	1	1	1	1	1	1
A_2	1	1	1	1	1	1	1	−1	−1
B_1	1	−1	1	−1	1	−1	1	1	−1
B_2	1	−1	1	−1	1	−1	1	−1	1
E_1	2	$\sqrt{3}$	1	0	−1	−$\sqrt{3}$	−2	0	0
E_2	2	1	−1	−2	−1	1	2	0	0
E_3	2	0	−2	0	2	0	−2	0	0
E_4	2	−1	−1	2	−1	−1	2	0	0
E_5	2	−$\sqrt{3}$	1	0	−1	$\sqrt{3}$	−2	0	0

TABLE V. Interlayer hybridization selection rules and classifications in twisted and untwisted BG systems. PG stands for the point group.

θ_t	PG	Selection rules	Hybridization classifications		
			Equivalent	Mixed	Nonequivalent
$\theta_t = 30°$	D_{6d}	$U_{A_i,A_j} = \delta_{A_i,A_j} U_{A_i,A_j}$ $U_{E_i,E_j} = \delta_{E_i,E_j} U_{E_i,E_j}$ $U_{B_1,ir'} = \delta_{B_2,ir'} U_{B_1,ir'}$ $U_{B_2,ir'} = \delta_{B_1,ir'} U_{B_2,ir'}$	$A_1 + A_1 \Rightarrow A_1 + B_2$ $A_2 + A_2 \Rightarrow A_2 + B_1$ $E_1 + E_1 \Rightarrow E_1 + E_5$ $E_2 + E_2 \Rightarrow E_2 + E_4$		$B_1 + B_2 \Rightarrow E_3 + E_3$ $B_2 + B_1 \Rightarrow E_3 + E_3$
$0° < \theta_t < 30°$	D_6	$U_{A_i,ir'} = (\delta_{A_1,ir'} + \delta_{A_2,ir'}) U_{A_i,ir'}$ $U_{B_i,ir'} = (\delta_{B_1,ir'} + \delta_{B_2,ir'}) U_{B_i,ir'}$ $U_{E_i,E_j} = \delta_{E_i,E_j} U_{E_i,E_j}$	$E_1 + E_1 \Rightarrow E_1 + E_1$ $E_2 + E_2 \Rightarrow E_2 + E_2$	$A_{1,2} + A_{1,2} \Rightarrow A_{1,2} + A_{2,1}$ $B_{1,2} + B_{1,2} \Rightarrow B_{1,2} + B_{2,1}$	
$\theta_t = 0°$	D_{6h}	$U_{ir,ir'} = \delta_{ir,ir'} U_{ir,ir'}$	$A_1 + A_1 \Rightarrow A_{1g} + A_{2u}$ $A_2 + A_2 \Rightarrow A_{2g} + A_{1u}$ $B_1 + B_1 \Rightarrow B_{2g} + B_{1u}$ $B_2 + B_2 \Rightarrow B_{1g} + B_{2u}$ $E_1 + E_1 \Rightarrow E_{1g} + E_{1u}$ $E_2 + E_2 \Rightarrow E_{2g} + E_{2u}$		

equations of $U_{ir,ir'}$ in Table V indicate which states of the two layers are allowed to be hybridized with each other, and hence enable a rule of the interlayer hybridization, namely, the *hybridization selection rule*. In graphene monolayer, states with two-dimensional (2D) irreps E_i are always degenerate and easily separated by the rotation operation C_6. Thus, we use C_6 to classify the eigenstates of each monolayer by virtue of $C_6|\varphi_{ir,\theta}^b\rangle = e^{i\theta}|\varphi_{ir,\theta}^b\rangle$ and $C_6|\varphi_{ir',\theta'}^t\rangle = e^{i\theta'}|\varphi_{ir',\theta'}^t\rangle$, where $\theta = 0$ for $ir = A_1$ and A_2, $\pm\pi/3$ for $ir = E_1$, π for $ir = B_1$ and B_2, and $\pm 2\pi/3$ for $ir = E_2$. In the basis functions of C_6, we write the hybridization matrix element as $U_{ir,ir'}^{\theta\theta'} = \delta_{\theta\theta'} U_{ir,ir'}^{\theta\theta'}$ because of

$$U_{ir,ir'}^{\theta\theta'} = \langle \varphi_{ir,\theta}^b | U | \varphi_{ir',\theta'}^t \rangle = \langle \varphi_{ir,\theta}^b | H | \varphi_{ir',\theta'}^t \rangle$$
$$= \langle \varphi_{ir,\theta}^b | C_6^\dagger H C_6 | \varphi_{ir',\theta'}^t \rangle = e^{i(\theta'-\theta)} U_{ir,ir'}^{\theta\theta'}. \quad (6)$$

IV. HYBRIDIZATION CLASSIFICATIONS AND HYBRIDIZATION STATES

In this paper, an interlayer hybridization process is labeled by $ir_b + ir_t \Rightarrow ir_+ + ir_-$, which describes that two pairing states from the bottom layer with irrep ir_b and the top layer with irrep ir_t are hybridized with each other and form the hybridization states with irreps ir_+ and ir_- of the bilayer system. Next, we will present the hybridization categories and the irreps of hybridization states generated by the interlayer hybridization in untwisted and twisted BGs. The derivations in detail are given in Appendix B and the results are summarized in Table V.

A. D_{6d} graphene quasicrystal

For the D_{6d} graphene quasicrystal, we derive the equivalent hybridizations

$$A_1 + A_1 \Rightarrow A_1 + B_2,$$
$$A_2 + A_2 \Rightarrow A_2 + B_1,$$
$$E_1 + E_1 \Rightarrow E_1 + E_5,$$
$$E_2 + E_2 \Rightarrow E_2 + E_4, \quad (7)$$

and the nonequivalent hybridizations

$$B_1 + B_2 \Rightarrow E_3 + E_3,$$
$$B_2 + B_1 \Rightarrow E_3 + E_3. \quad (8)$$

For the equivalent hybridization $ir + ir \Rightarrow ir_+ + ir_-$ with $ir = A_1$, A_2, E_1, and E_2, the hybridization states with irreps ir_+ and ir_- states can be written as

$$|\phi_\pm^{ir}\rangle = \frac{1}{\sqrt{2}}\left(e^{i\frac{\theta}{2}}|\varphi_{ir}^b\rangle \pm S_{12}|\varphi_{ir}^b\rangle\right), \quad (9)$$

where $|\varphi_{ir}^b\rangle$ is the eigenstate of rotation C_6 from the bottom layer with $C_6|\varphi_{ir}^b\rangle = e^{i\theta}|\varphi_{ir}^b\rangle$. Using $S_{12}S_{12} = C_6$, we have $S_{12}|\phi_\pm^{ir}\rangle = \pm e^{i\frac{\theta}{2}}|\phi_\pm^{ir}\rangle$, which indicates that the states $|\phi_\pm^{ir}\rangle$ generated by equivalent hybridization are 12-fold symmetrical. For nonequivalent hybridizations, the hybridization states $|\phi_\pm^{E_3}\rangle$ are not the eigenstates for S_{12} but for C_6, and hence $|\phi_\pm^{E_3}\rangle$ are sixfold symmetrical.

B. D_6 twisted bilayer graphene

For twisted BGs with D_6 symmetries, we derive the mixed hybridizations

$$A_{1,2} + A_{1,2} \Rightarrow A_{1,2} + A_{2,1},$$
$$B_{1,2} + B_{1,2} \Rightarrow B_{1,2} + B_{2,1}, \quad (10)$$

and the equivalent hybridizations

$$E_1 + E_1 \Rightarrow E_1 + E_1,$$
$$E_2 + E_2 \Rightarrow E_2 + E_2. \quad (11)$$

The mixed hybridization can be viewed as a mixture of two equivalent hybridizations. For instance, the mixed hybridization $A_{1,2} + A_{1,2} \Rightarrow A_{1,2} + A_{2,1}$ can be rewritten as two equivalent hybridizations

$$A_1 + A_1 \Rightarrow A_1 + A_2,$$
$$A_2 + A_2 \Rightarrow A_2 + A_1, \quad (12)$$

and then the two A_1 (A_2) states on the right side of Eq. (12) are coupled together to form the eigenstates of the D_6 twisted BG.
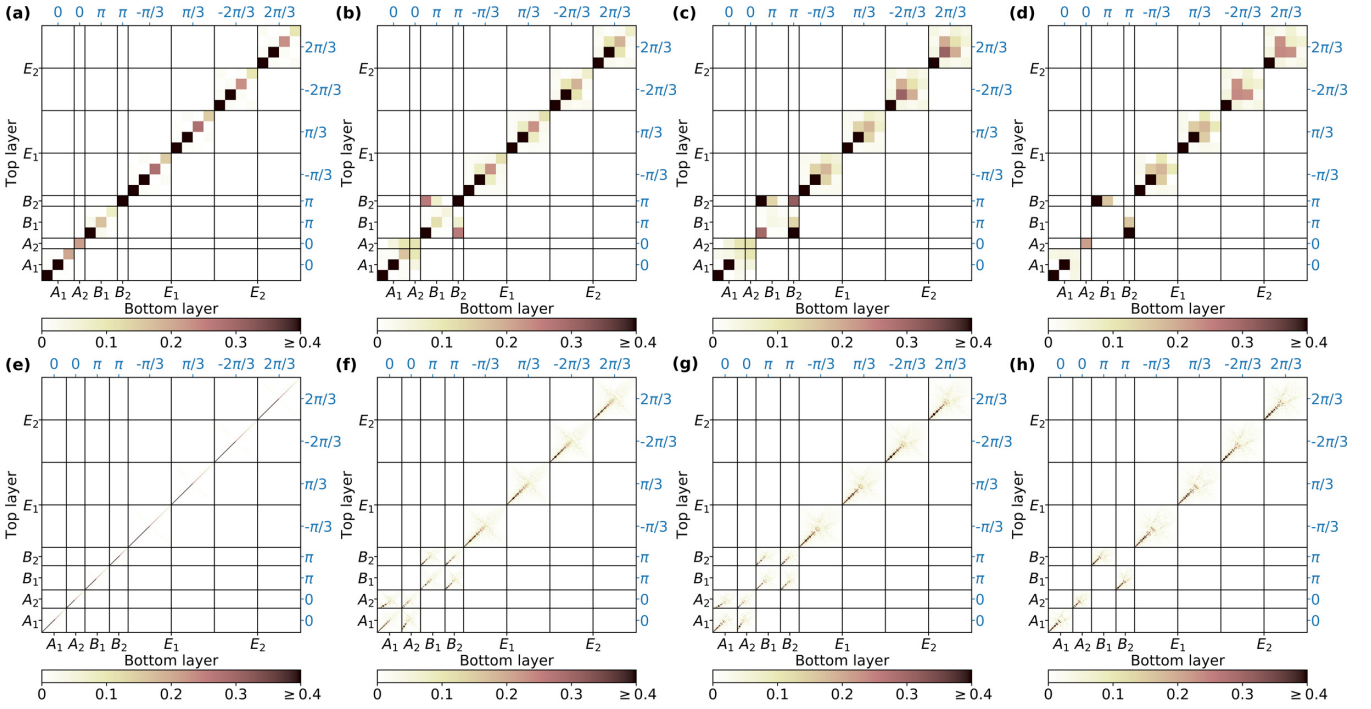
FIG. 2. Interlayer hybridization matrix elements with their absolute values $|\langle\varphi^b_{ir,\theta}|U|\varphi^t_{ir',\theta'}\rangle|$ in units of eV at (a), (e) $\theta_t = 0°$, (b), (f) $\theta_t = 10°$, (c), (g) $\theta_t = 20°$, and (d), (h) $\theta_t = 30°$ for (size 2, size 8) twisted BG quantum dots from p_z-orbital-based TB model. These eigenstates of the two layers $|\varphi^b_{ir,\theta}\rangle$ and $|\varphi^t_{ir',\theta'}\rangle$ are classified by the irreps of C_{6v} and θ in the eigenvalue $e^{i\theta}$ of rotation operation C_6.

The same procedure is also suitable for $B_{1,2} + B_{1,2} \Rightarrow B_{1,2} + B_{2,1}$, which is a mixture of two equivalent hybridizations

$$B_1 + B_1 \Rightarrow B_1 + B_2,$$
$$B_2 + B_2 \Rightarrow B_2 + B_1. \tag{13}$$

For one equivalent hybridization or the equivalent part of one mixed hybridizations $ir + ir \Rightarrow ir_+ + ir_-$, the hybridization states with irreps ir_+ and ir_- states can be written as

$$\left|\phi^{ir}_\pm\right\rangle = \frac{1}{\sqrt{2}}\left(\left|\varphi^b_{ir}\right\rangle \pm \sigma_h R(\theta_t)\left|\varphi^b_{ir}\right\rangle\right). \tag{14}$$

C. D_{6h} untwisted BG

For AA-stacked BG, we derive only equivalent hybridizations

$$A_1 + A_1 \Rightarrow A_{1g} + A_{2u},$$
$$A_2 + A_2 \Rightarrow A_{2g} + A_{1u},$$
$$B_1 + B_1 \Rightarrow B_{2g} + B_{1u},$$
$$B_2 + B_2 \Rightarrow B_{1g} + B_{2u},$$
$$E_1 + E_1 \Rightarrow E_{1g} + E_{1u},$$
$$E_2 + E_2 \Rightarrow E_{2g} + E_{2u}. \tag{15}$$

The hybridization states with irreps ir_+ and ir_- states can be written as

$$\left|\phi^{ir}_\pm\right\rangle = \frac{1}{\sqrt{2}}\left(\left|\varphi^b_{ir}\right\rangle \pm \sigma_h\left|\varphi^b_{ir}\right\rangle\right). \tag{16}$$

D. D_{3d} AB-stacked BG

Although AB-stacked BG can not be obtained by rotating the top layer as shown in Fig. 1, we also here discuss briefly its interlayer hybridizations. For AB-stacked BG, the system has the D_{3d} symmetry consisting of two C_{3v} monolayers. After symmetry analyses and algebraic evaluations we find that there are only equivalent hybridizations

$$A_1 + A_1 \Rightarrow A_{1g} + A_{2u},$$
$$A_2 + A_2 \Rightarrow A_{2g} + A_{1u},$$
$$E + E \Rightarrow E_g + E_u. \tag{17}$$

V. NUMERICAL VERIFICATION OF HYBRIDIZATION SELECTION RULES

The hybridization selection rules in Table V are the result of symmetries no matter the system size. We consider finite-size twisted BG structures with the same point-group symmetries as those of the infinite-size systems to identify the interlayer hybridization selection rules by the numerical calculations of the hybridization matrix elements. We note that the finite-size-induced additional changes to the symmetry are not included here. The twisted BG quantum dots customized as shown in Fig. 1 are adopted to verify the interlayer hybridization selection rules. For size-2 and size-8 twisted BG quantum dots at $\theta_t = 0°, 10°, 20°$, and $30°$, the p_z- and Wannier-orbital-based TB models (see Appendixes C and D) are used to calculate the hybridization matrix elements, and the results are shown in Figs. 2 and 3. The hybridization and overlap matrix elements of size-2 twisted BGs at $\theta_t = 0°, 10°, 20°$, and $30°$ are obtained by DFT calculations
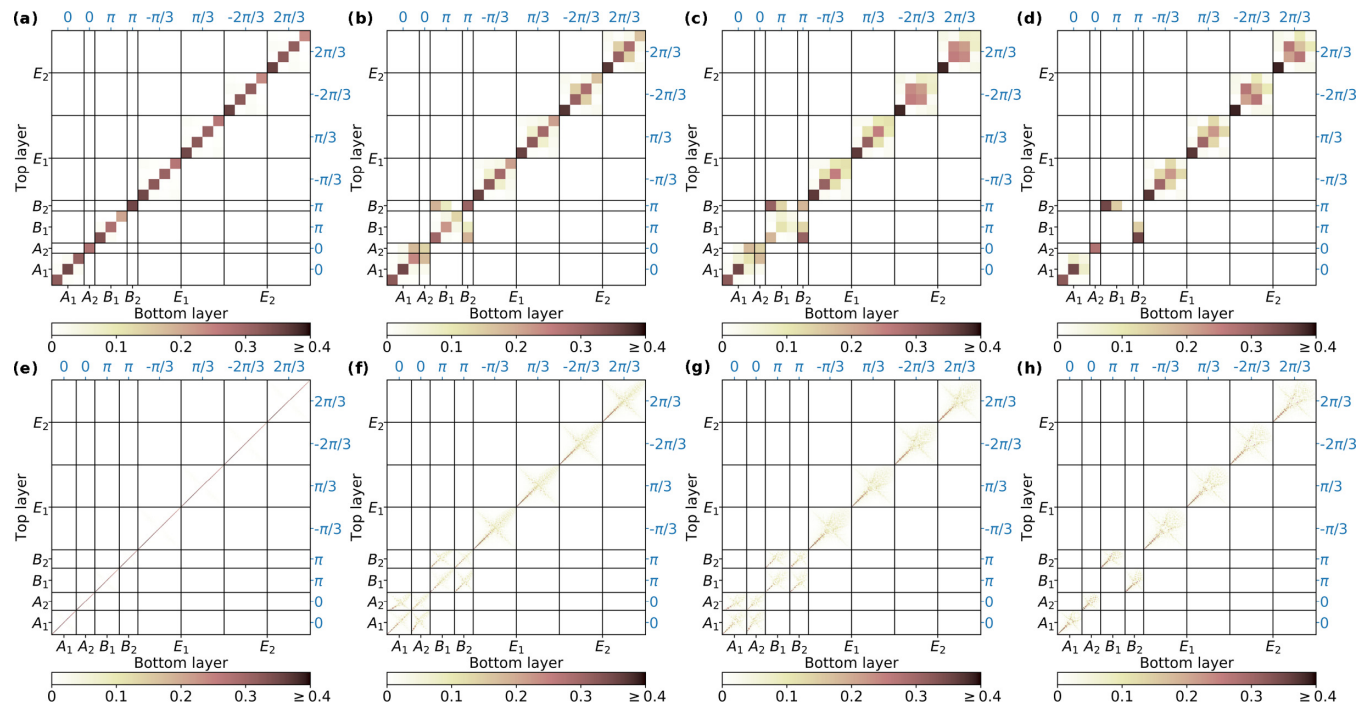
FIG. 3. Interlayer hybridization matrix elements with their absolute values $|\langle\varphi^b_{ir,\theta}|U|\varphi^t_{ir',\theta'}\rangle|$ in units of eV at (a), (e) $\theta_t = 0°$, (b), (f) $\theta_t = 10°$, (c), (g) $\theta_t = 20°$, and (d), (h) $\theta_t = 30°$ for (size-2, size-8) twisted BG quantum dots from Wannier-orbital-based TB model. These eigenstates of the two layers $|\varphi^b_{ir,\theta}\rangle$ and $|\varphi^t_{ir',\theta'}\rangle$ are classified by the irreps of C_{6v} and θ in the eigenvalue $e^{i\theta}$ of rotation operation C_6.

(see Appendix E), and the results are shown in Fig. 4. The mapped distributions of these nonzero hybridization matrix elements with $U^{\theta\theta'}_{ir,ir'} \neq 0$ from the three different methods manifest the hybridization selection rules of BG structures in
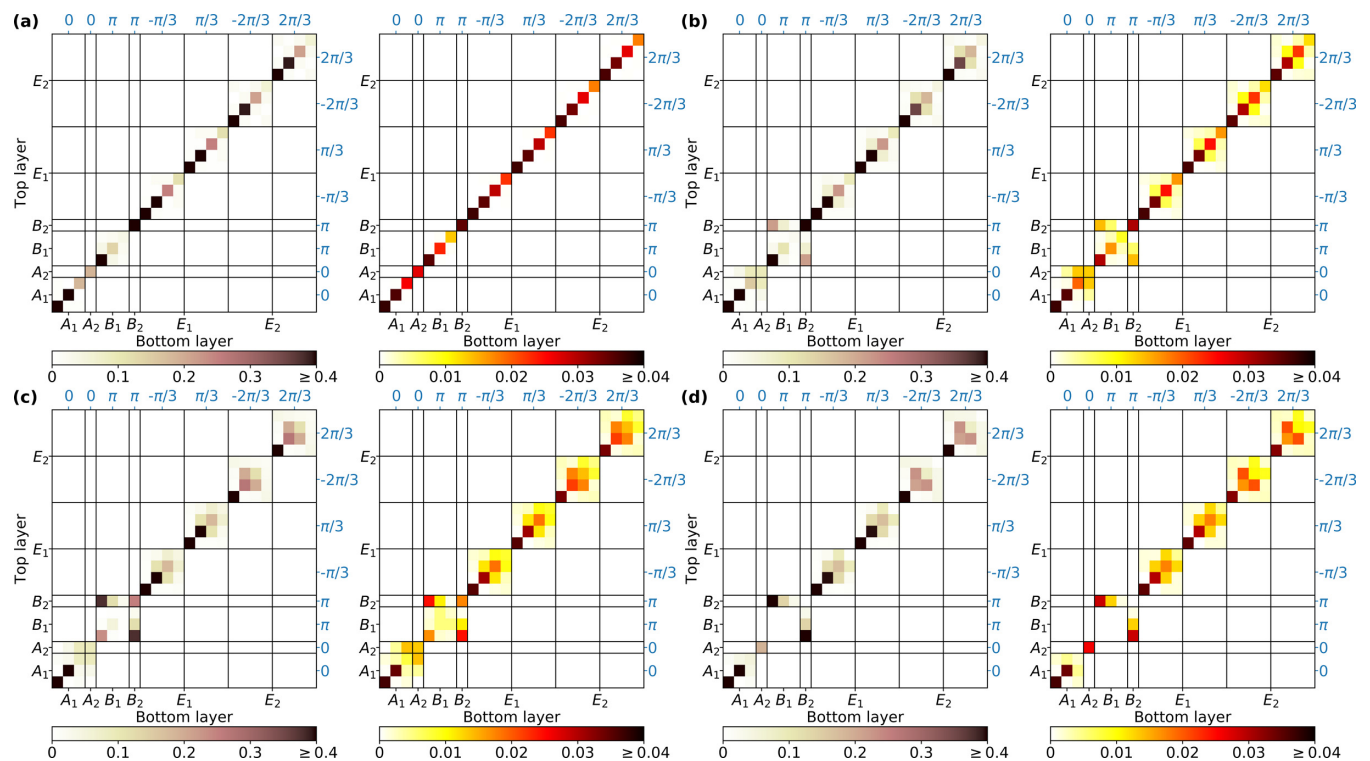

FIG. 4. Interlayer hybridization matrix elements (left panel in each subplot) and overlap matrix elements (right panel in each subplot) with their absolute values $|\langle\varphi^b_{ir,\theta}|U|\varphi^t_{ir',\theta'}\rangle|$ and $|\langle\varphi^b_{ir,\theta}|\varphi^t_{ir',\theta'}\rangle|$ in units of eV at (a) $\theta_t = 0°$, (b) $\theta_t = 10°$, (c) $\theta_t = 20°$, and (d) $\theta_t = 30°$ for size-2 twisted BG quantum dots from DFT calculations. These eigenstates of the two layers $|\varphi^b_{ir,\theta}\rangle$ and $|\varphi^t_{ir',\theta'}\rangle$ are classified by the irreps of C_{6v} and θ in the eigenvalue $e^{i\theta}$ of rotation operation C_6.
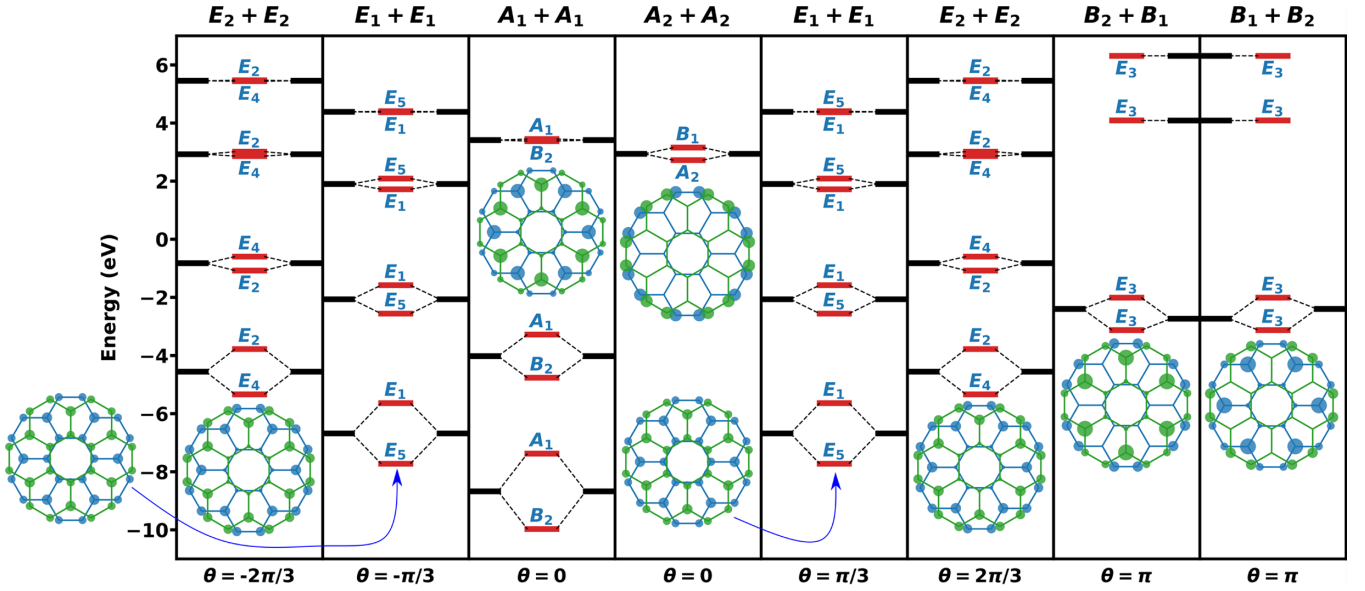
FIG. 5. The interlayer hybridizations for size-2 graphene quasicrystal quantum dot. Each subplot stands for one hybridization labeled by $ir_b + ir_t$ above. The energy levels of the pairing states of the bottom and top C_{6v} monolayers are correspondingly denoted by the left and right black lines. The energy levels of the hybridization states of the D_{6d} bilayer system are denoted by the middle red lines. The insets show the real-space electron density (denoted by the circle size) for these states nearest above the insets themselves or indicated by the blue arrows. The value of θ labeled below in each subplot corresponds to the eigenvalue of C_6, i.e., $C_6|\varphi_{ir}^{b/t}\rangle = e^{i\theta}|\varphi_{ir}^{b/t}\rangle$.

Table V. As an example, Fig. 5 shows the eigenenergy spectra and their irreps in the size-2 graphene quasicrystal quantum dot calculated by p_z-orbital-based TB model. These interlayer hybridizations follow the selection rules of graphene quasicrystal. Furthermore, the electron density distributions in the insets of Fig. 5 verify the 12-fold rotational symmetry of hybridization states from equivalent hybridizations and the sixfold rotational symmetry for hybridization states from nonequivalent hybridizations.

VI. HYBRIDIZATION STRENGTHS

Following the interlayer hybridization rules, we can determine which states of the two monolayers can be hybridized with each other. For an arbitrary eigenstate $|\phi\rangle$ of twisted BG with energy ε, we can write $|\phi\rangle$ as $c|\varphi^b\rangle + d|\varphi^t\rangle$, with normalized components $|\varphi^b\rangle$ and $|\varphi^t\rangle$ from the bottom and top layers and $|c|^2 + |d|^2 = 1$. To measure the energy-dependent interlayer coupling strength, we define the hybridization strength for $|\phi\rangle$ as

$$\Delta\varepsilon = \begin{cases} \varepsilon - \max(\bar{\varepsilon}_b, \bar{\varepsilon}_t), & \text{if } \varepsilon > \max(\bar{\varepsilon}_b, \bar{\varepsilon}_t), \\ \varepsilon - \min(\bar{\varepsilon}_b, \bar{\varepsilon}_t), & \text{if } \varepsilon < \min(\bar{\varepsilon}_b, \bar{\varepsilon}_t), \end{cases} \quad (18)$$

where $\bar{\varepsilon}_b = \langle\varphi^b|H_0^b|\varphi^b\rangle$ and $\bar{\varepsilon}_t = \langle\varphi^t|H_0^t|\varphi^t\rangle$ are the energy averages of states $|\varphi^b\rangle$ and $|\varphi^t\rangle$. The state $|\phi\rangle$ corresponding to the first (second) case with positive (negative) $\Delta\varepsilon$ is defined as the antibonding (bonding) state. To see how the interlayer hybridizations vary on the energy, we use the p_z-orbital-based TB model to numerically compute the hybridization strength as a function of energy for graphene quasicrystal structures with size 10, size 20, and infinite size approximated by the periodic 15/26 approximant [31], AA-stacked BG, and other twisted BGs with various twist angles. The calculated

results are shown in Fig. 6. As we can see, the energy-dependent hybridization strength shows two characteristics:
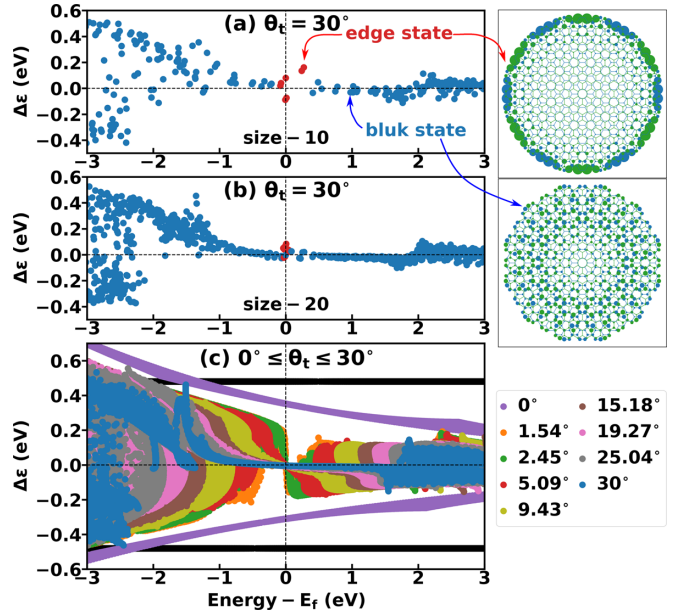

FIG. 6. The hybridization strengths as a function of energy for dodecagonal graphene quasicrystal structures with size 10 in (a) and size 20 in (b) and for other infinite-size twisted BG systems with various twist angles in (c), where the size-∞ quasicrystal is calculated using a periodic 15/26 approximant [31], and the two black lines represent the hybridization strengths of AA-stacked BG only with the nearest-neighbor interlayer hopping. The right two insets show the real-space electron density for the signaled states indicated by arrows in (a).

(i) the hybridization strengths in twisted BG are weak near the Fermi level except for the edge states denoted by red dots in Figs. 6(a) and 6(b) with localized electron density at the edges and the hybridization states in AA-stacked BG in Fig. 6(c), and (ii) an electron-hole asymmetry of hybridization strength with stronger interlayer coupling for holes appears in higher-energy areas in Fig. 6(c). The calculated weak interlayer hybridization strengths inside the low-energy area verify that graphene quasicrystal has a similar low-energy dispersion as that of a decoupled graphene bilayer [17,18,24,38,39]. Next, we will discuss the two characteristics of energy-dependent hybridization strengths in these systems.

A. Weak hybridization strengths near the Fermi level

This weak hybridization strength near the Fermi level can be understood by the perturbation theory. We first express the interlayer Hamiltonian matrix elements based on the Bloch bases. Within the p_z-orbital-based TB model for both untwisted BG and twisted BG, the Bloch bases of the two monolayers are defined as

$$
|k^b, X^b\rangle = \frac{1}{\sqrt{N}} \sum_{L^b} e^{ik^b \cdot (L^b + \tau^b_{X^b})} |L^b + \tau^b_{X^b}\rangle,
$$
$$
|k^t, X^t\rangle = \frac{1}{\sqrt{N}} \sum_{L^t} e^{ik^t \cdot (L^t + \tau^t_{X^t})} |L^t + \tau^t_{X^t}\rangle,
$$
(19)

where N is the normalization factor, $L^b = n_1^b a_1^b + n_2^b a_2^b$ ($L^t = n_1^t a_1^t + n_2^t a_2^t$) is the unit-cell vector, and $|L^b + \tau^b_{X^b}\rangle$ ($|L^t + \tau^t_{X^t}\rangle$) denotes the p_z orbital located at sublattice X^b (X^t) in unit cell L^b (L^t). The intralayer Hamiltonian matrix elements read as

$$
\langle k^b, X^b | H_0^b | k^{b'}, X^{b'} \rangle = \delta_{k^b k^{b'}} \sum_{L^b} t(L^b + \tau^b_{X^{b'} X^b}) e^{ik^b \cdot (L^b + \tau^b_{X^{b'} X^b})},
$$
$$
\langle k^t, X^t | H_0^t | k^{t'}, X^{t'} \rangle = \delta_{k^t k^{t'}} \sum_{L^t} t(L^t + \tau^t_{X^{t'} X^t}) e^{ik^t \cdot (L^t + \tau^t_{X^{t'} X^t})},
$$
(20)

where $\tau^b_{X^{b'} X^b} = \tau^b_{X^{b'}} - \tau^b_{X^b}$ and $\tau^t_{X^{t'} X^t} = \tau^t_{X^{t'}} - \tau^t_{X^t}$. The interlayer Hamiltonian matrix elements read as [27,33,40]

$$
\langle k^b, X^b | U | k^t, X^t \rangle = \sum_{G^b G^t} T(|k^b + G^b|) e^{iG^b \cdot \tau^b_{X^b}} e^{-iG^t \cdot \tau^t_{X^t}} \delta_{k^b + G^b, k^t + G^t},
$$
(21)

where $T(|k^b + G^b|)$ is the xy-plane Fourier transform of interlayer hopping function $t(r_{xy} + h\hat{e}_z)$ at $k^b + G^b$. Here $G^b = m^b b_1^b + n^b b_2^b$ and $G^t = m^t b_1^t + n^t b_2^t$ run over all of the reciprocal points of the bottom and top layers, respectively, with $b_1^{b/t}$ and $b_2^{b/t}$ being the reciprocal lattice vectors of the two layers. The in-plane Fourier transform $T(q)$ of the interlayer hopping $t(r)$ at q is defined as

$$
T(q) = \frac{1}{S} \int t(r_{xy} + h\hat{e}_z) e^{-iq \cdot r_{xy}} dr_{xy},
$$
(22)

where S is the area of the unit cell in graphene, and $\hat{e}_z$ is the unit vector along the z axis. $T(q) = T(|q|)$ depends on only the length of q for the p_z-orbital-based TB model. Equation (21) indicates that the interlayer Hamiltonian matrix elements are nonzero only for the Bloch bases of the two monolayers with the wave vectors satisfying $k^b + G^b = k^t + G^t$. This wave-vector-dependent interlayer coupling condition $k^b + G^b = k^t + G^t$ can be rewritten as [41–43]

$$
k^b - k^t = mg_1 + ng_2,
$$
(23)

where m and n are two arbitrary integer values, and g_1 and g_2 take the forms as

$$
g_1 = b_1^b - b_1^t,
$$
$$
g_2 = b_2^b - b_2^t.
$$
(24)

We now consider a commensurate twisted BG with $\theta_t = 9.43°$ as an example to illustrate the weak interlayer hybridization strengths near the Fermi level. Figure 7 shows the Brillouin zones of this twisted BG and its two layers. According to the wave-vector-dependent interlayer coupling condition in Eqs. (23) and (24), the Dirac point K^b of the bottom layer can couple with the k^t points of the top layer mainly at $k^t = K^b + 0, k^t = K^b + g_1$, and $k^t = K^b - g_2$, and the coupling strengths between K^b and the above three k^t points are the same, i.e., $T(|K^b|) \sim 0.11$ eV [7,44]. The corresponding hybridization-generated band structures together with hybridization strengths are plotted in Fig. 8(a), where the color represents the interlayer hybridization strength $\Delta\varepsilon$ in Eq. (18), and the black dashed lines represent the Dirac band structures of the Hamiltonians H_0^b and H_0^t of graphene monolayers. As we can see, the hybridization strengths around K^b and K^t (near the Fermi level) are indeed weak and the hybridization strengths around M point inside relatively high-energy areas are obviously stronger in Fig. 8(a). The weak hybridization strength near the Fermi level can be well explained by the second-order nondegenerate perturbation theory. The first-order energy correction is $E_n^{(1)} = \langle\varphi_n^{(0)}|U|\varphi_n^{(0)}\rangle$ with the wave function of ground state $|\varphi_n^{(0)}\rangle$ of unperturbed Hamiltonian H_0, and the second-order energy correction $E_n^{(2)}$ reads as

$$
E_n^{(2)} = \sum_{m \neq n} \frac{|\langle\varphi_m^{(0)}|U|\varphi_n^{(0)}\rangle|^2}{E_n^{(0)} - E_m^{(0)}}.
$$
(25)

The wave-vector-dependent interlayer coupling conditions in Eqs. (23) and (24) indicate the direct interlayer couplings between $k^b = K^b$ and $k^t = K^t$ points are not allowed, i.e., the first-order energy correction $E_n^{(1)}$ is zero. Around K^b and K^t,
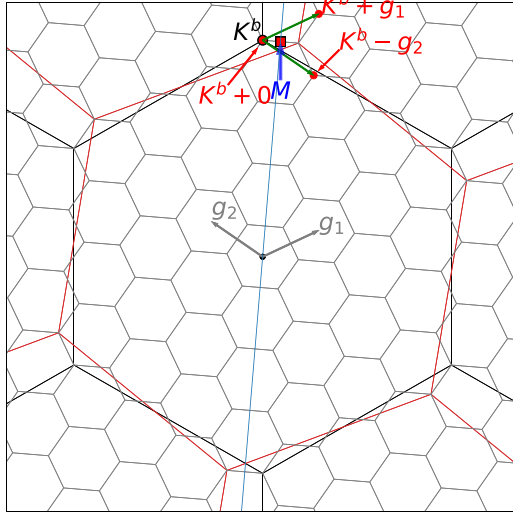
FIG. 7. Brillouin zones of twisted BG with $\theta_t = 9.43°$ and its two layers. Black and red big hexagons are the Brillouin zones of the bottom and top graphene, respectively. Gray hexagon network is the Brillouin zone of twisted BG with g_1 and g_2 as its reciprocal lattice vectors. The wave-vector-dependent interlayer coupling condition in Eqs. (23) and (24) requires that the Bloch function from the bottom layer at $k^b = K^b$ mainly couple with three Bloch functions from the top layer at $k^t = K^b + 0$, $K^b + g_1$, and $K^b - g_2$. If the equal wave vectors k^b and k^t are on the blue dashed line across M point, the Bloch bases of the two monolayers have the same energy. On the blue dashed line, M point is closest to the Dirac points K^b and K^t.

the energy differences between the two Dirac linear bands (denoted by dashed lines) are about 1.33 and 1.49 eV in Fig. 8(a), and the coupling strength $|\langle \varphi_m^{(0)}|U|\varphi_n^{(0)}\rangle|$ is 0.11 eV [7,44], and hence the second-order energy correction $E_n^{(2)}$ will be very small in Eq. (25). Consequently, the hybridization strength is very weak near the Fermi level.

For these k points on the blue dashed line in Fig. 7, the states from the two monolayers have the same energy, and the first-order degenerate perturbation theory can be applied to illustrate the relatively large hybridization strength near the blue dashed line. According to the first-order degenerate perturbation theory, the original degenerate energy bands are
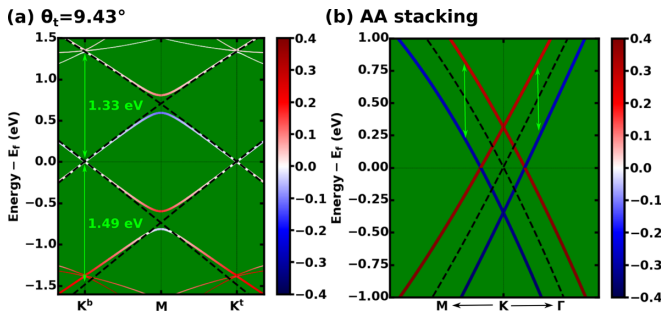

FIG. 8. (a) The calculated unfolded band structures for twisted BG with $\theta_t = 9.43°$ and (b) the calculated band structures for AA-stacked BG, where the color denotes the interlayer hybridization strength $\triangle \varepsilon$, and the black dashed lines stand for the band structures of the bottom and top graphene monolayers.
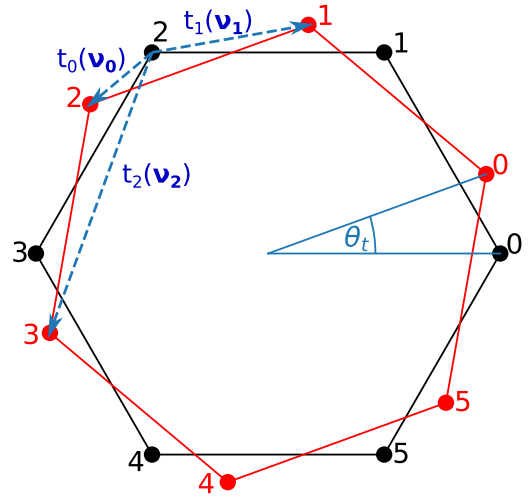

FIG. 9. Two six-carbon rings with a twist angle of θ_t, where the bottom and top rings are denoted by black and red colors, respectively, t_0, t_1, and t_2 are the interlayer NN, NNN, and TNN hoppings, respectively, and ν_0, ν_1, and ν_2 are the interlayer NN, NNN, and TNN displacements, respectively.

split, and hence the hybridization strength is relatively large, such as the hybridization strength (denoted by the color) around M point in Fig. 8(a). For AA-stacked BG, the energy bands (dashed lines) for the top and bottom monolayers are always degenerate at all k points, and hence the degenerate energy bands are split with the energy difference denoted by the green double arrows and the relatively large hybridization strength at each k point, as shown in Fig. 8(b), as a result of the first-order degenerate perturbation theory.

B. Electron-hole asymmetrical hybridization strength inside high-energy area

We first use a toy model of two six-carbon rings in Fig. 9 as a starting point to seek an expression of interlayer hybridization strengths and then generalize the expression of interlayer hybridization strengths in an arbitrary BG system. The Hamiltonian of the twisted two six-carbon rings reads as

$$H = \begin{bmatrix} H_0^b & U \\ U^\dagger & H_0^t \end{bmatrix}, \qquad (26)$$

where H_0^b and H_0^t are the Hamiltonians of the bottom and top rings, respectively, and U is the interlayer coupling. For simplicity, we consider the nearest-neighbor (NN) approximation within the monolayers and write H_0^b and H_0^t as

$$H_0^b = H_0^t = \begin{bmatrix} 0 & -t & 0 & 0 & 0 & -t \\ -t & 0 & -t & 0 & 0 & 0 \\ 0 & -t & 0 & -t & 0 & 0 \\ 0 & 0 & -t & 0 & -t & 0 \\ 0 & 0 & 0 & -t & 0 & -t \\ -t & 0 & 0 & 0 & -t & 0 \end{bmatrix}, \qquad (27)$$

where $-t$ is the in-plane NN hopping energy. The U within the third-nearest-neighbor (TNN) approximation of the interlayer

hoppings is written as

$$
U = \begin{bmatrix} t_0(\boldsymbol{v}_0) & t_2(\boldsymbol{v}_2) & 0 & 0 & 0 & t_1(\boldsymbol{v}_1) \\ t_1(\boldsymbol{v}_1) & t_0(\boldsymbol{v}_0) & t_2(\boldsymbol{v}_2) & 0 & 0 & 0 \\ 0 & t_1(\boldsymbol{v}_1) & t_0(\boldsymbol{v}_0) & t_2(\boldsymbol{v}_2) & 0 & 0 \\ 0 & 0 & t_1(\boldsymbol{v}_1) & t_0(\boldsymbol{v}_0) & t_2(\boldsymbol{v}_2) & 0 \\ 0 & 0 & 0 & t_1(\boldsymbol{v}_1) & t_0(\boldsymbol{v}_0) & t_2(\boldsymbol{v}_2) \\ t_2(\boldsymbol{v}_2) & 0 & 0 & 0 & t_1(\boldsymbol{v}_1) & t_0(\boldsymbol{v}_0) \end{bmatrix},
$$

$$(28)$$

where $t_0(\boldsymbol{v}_0)$, $t_1(\boldsymbol{v}_1)$, and $t_2(\boldsymbol{v}_2)$ are the NN, next-nearest-neighbor (NNN), and TNN interlayer hoppings, respectively, as shown in Fig. 9. From Eqs. (C1) and (C2), one can find that all $t_0(\boldsymbol{v}_0)$, $t_1(\boldsymbol{v}_1)$, and $t_2(\boldsymbol{v}_2)$ are positive. In addition, for untwisted case with $\theta_t = 0°$, $t_0(\boldsymbol{v}_0) > t_1(\boldsymbol{v}_1) = t_2(\boldsymbol{v}_2) > 0$, and for $\theta_t = 30°$, $t_0(\boldsymbol{v}_0) = t_1(\boldsymbol{v}_1) \gg t_2(\boldsymbol{v}_2) \sim 0$. The real eigenvalues ϵ and eigenvectors ψ for H_0^b and H_0^t in Eq. (27)

read as

$$
A_1, \ \epsilon = -2t: \quad \psi_0^{b/t} = \frac{1}{\sqrt{6}}(1, 1, 1, 1, 1, 1)^T,
$$

$$
E_1, \ \epsilon = -t: \quad \psi_1^{b/t} = \frac{1}{2}(-1, -1, 0, 1, 1, 0)^T,
$$

$$
E_1, \ \epsilon = -t: \quad \psi_2^{b/t} = \frac{1}{2}(1, 0, -1, -1, 0, 1)^T,
$$

$$
E_2, \ \epsilon = t: \quad \psi_3^{b/t} = \frac{1}{2}(-1, 1, 0, -1, 1, 0)^T,
$$

$$
E_2, \ \epsilon = t: \quad \psi_4^{b/t} = \frac{1}{2}(-1, 0, 1, -1, 0, 1)^T,
$$

$$
B_1, \ \epsilon = 2t: \quad \psi_5^{b/t} = \frac{1}{\sqrt{6}}(-1, 1, -1, 1, -1, 1)^T. \tag{29}
$$

Within the basis function of rotation operation C_6, we rewrite the eigenvectors as

$$
A_1, \ \theta = 0, \ \epsilon = -2t: \quad \phi_0^{b/t} = \psi_0^{b/t} = \frac{1}{\sqrt{6}}(1, 1, 1, 1, 1, 1)^T,
$$

$$
E_1, \ \theta = -\frac{\pi}{3}, \ \epsilon = -t: \quad \phi_1^{b/t} = \frac{2}{\sqrt{6}}\big(e^{-i\frac{\pi}{3}}\psi_1^{b/t} + \psi_2^{b/t}\big) = \frac{1}{\sqrt{6}}(e^{i\frac{\pi}{3}}, e^{i\frac{2\pi}{3}}, e^{i\pi}, e^{-i\frac{2\pi}{3}}, e^{-i\frac{\pi}{3}}, e^{i0})^T,
$$

$$
E_1, \ \theta = \frac{\pi}{3}, \ \epsilon = -t: \quad \phi_2^{b/t} = \frac{2}{\sqrt{6}}\big(e^{i\frac{\pi}{3}}\psi_1^{b/t} + \psi_2^{b/t}\big) = \frac{1}{\sqrt{6}}(e^{-i\frac{\pi}{3}}, e^{-i\frac{2\pi}{3}}, e^{i\pi}, e^{i\frac{2\pi}{3}}, e^{i\frac{\pi}{3}}, e^{i0})^T, \tag{30}
$$

and

$$
E_2, \ \theta = -\frac{2\pi}{3}, \ \epsilon = t: \quad \phi_3^{b/t} = \frac{2}{\sqrt{6}}\big(e^{-i\frac{2\pi}{3}}\psi_3^{b/t} + \psi_4^{b/t}\big) = \frac{1}{\sqrt{6}}(e^{i\frac{2\pi}{3}}, e^{-i\frac{2\pi}{3}}, e^{i0}, e^{i\frac{2\pi}{3}}, e^{-i\frac{2\pi}{3}}, e^{i0})^T,
$$

$$
E_2, \ \theta = \frac{2\pi}{3}, \ \epsilon = t: \quad \phi_4^{b/t} = \frac{2}{\sqrt{6}}\big(e^{i\frac{2\pi}{3}}\psi_3^{b/t} + \psi_4^{b/t}\big) = \frac{1}{\sqrt{6}}(e^{-i\frac{2\pi}{3}}, e^{i\frac{2\pi}{3}}, e^{i0}, e^{-i\frac{2\pi}{3}}, e^{i\frac{2\pi}{3}}, e^{i0})^T,
$$

$$
B_1, \ \theta = \pi, \ \epsilon = 2t: \quad \phi_5^{b/t} = \psi_5^{b/t} = \frac{1}{\sqrt{6}}(-1, 1, -1, 1, -1, 1)^T, \tag{31}
$$

where θ is related to the eigenvalue of C_6, i.e., $C_6\phi_i^{b/t} = e^{i\theta}\phi_i^{b/t}$. Using Eqs. (30) and (31) and the hybridization selection rule in Table V, we can write a uniform formula for the monolayer state as $\phi^{b/t} = (a_0^{b/t}, a_1^{b/t}, a_2^{b/t}, a_3^{b/t}, a_4^{b/t}, a_5^{b/t})^T$ with $\sum_{i=0}^5 |a_i^{b/t}|^2 = 1$. The interlayer bonding ($-$) and antibonding ($+$) states for each interlayer hybridization read as

$$
\varphi_- = \frac{1}{\sqrt{2}}\begin{pmatrix} \phi^b \\ -\phi^t \end{pmatrix} = \frac{1}{\sqrt{2}}(a_0^b, a_1^b, a_2^b, a_3^b, a_4^b, a_5^b, -a_0^t, -a_1^t, -a_2^t, -a_3^t, -a_4^t, -a_5^t)^T,
$$

$$
\varphi_+ = \frac{1}{\sqrt{2}}\begin{pmatrix} \phi^b \\ \phi^t \end{pmatrix} = \frac{1}{\sqrt{2}}(a_0^b, a_1^b, a_2^b, a_3^b, a_4^b, a_5^b, a_0^t, a_1^t, a_2^t, a_3^t, a_4^t, a_5^t)^T. \tag{32}
$$

The energy for bonding ($-$) and antibonding ($+$) states read as

$$
\varepsilon_\pm = \varphi_\pm^\dagger H \varphi_\pm = \tfrac{1}{2}[\phi^b]^\dagger H_0^b \phi^b + \tfrac{1}{2}[\phi^t]^\dagger H_0^t \phi^t \pm \tfrac{1}{2}[\phi^b]^\dagger U \phi^t \pm \tfrac{1}{2}[\phi^t]^\dagger U^\dagger \phi^b = \tfrac{1}{2}\varepsilon^b + \tfrac{1}{2}\varepsilon^t \pm \tfrac{1}{2}[\phi^b]^\dagger U \phi^t \pm \tfrac{1}{2}[\phi^t]^\dagger U^\dagger \phi^b. \tag{33}
$$

Then, the corresponding interlayer hybridization strengths for the two states are

$$
\Delta\varepsilon_- = -\tfrac{1}{2}[\phi^b]^\dagger U \phi^t - \tfrac{1}{2}[\phi^t]^\dagger U^\dagger \phi^b,
$$

$$
\Delta\varepsilon_+ = \tfrac{1}{2}[\phi^b]^\dagger U \phi^t + \tfrac{1}{2}[\phi^t]^\dagger U^\dagger \phi^b, \tag{34}
$$

where $[\phi^b]^\dagger U \phi^t$ and $[\phi^t]^\dagger U^\dagger \phi^b$ take the form as

$$
[\phi^b]^\dagger U \phi^t = \sum_{i=0}^5 t_0(\boldsymbol{v}_0)\big(a_i^{b*} a_i^t\big) + t_1(\boldsymbol{v}_1)\big(a_0^{b*} a_5^t + a_1^{b*} a_0^t + a_2^{b*} a_1^t + a_3^{b*} a_2^t + a_4^{b*} a_3^t + a_5^{b*} a_4^t\big)
$$

$$
+ t_2(\boldsymbol{v}_2)\big(a_0^{b*} a_1^t + a_1^{b*} a_2^t + a_2^{b*} a_3^t + a_3^{b*} a_4^t + a_4^{b*} a_5^t + a_5^{b*} a_0^t\big),
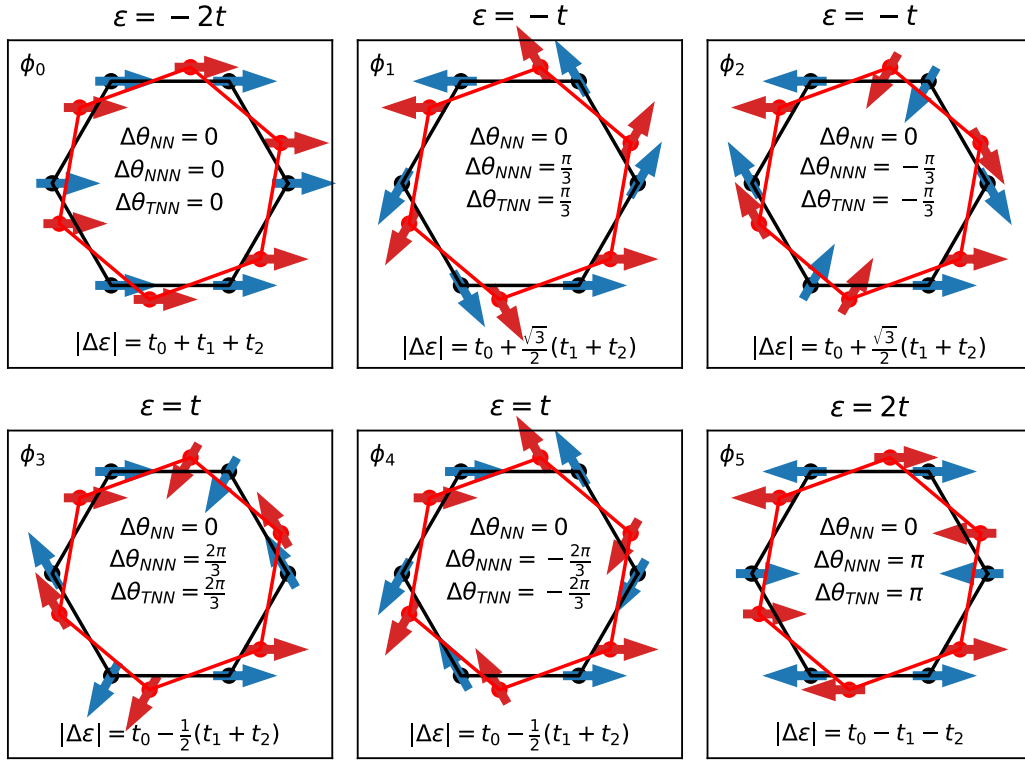$$

FIG. 10. Phases of 12 eigenstates $\phi_i^{b/t}$ (with $i = 0, \ldots, 5$, and $\phi_i^{b/t} = \phi_i$) in Eqs. (30) and (31) for the two six-carbon rings with a twist angle of θ_t. The wave-function phase difference of pairing states $\phi_i^{b/t}$ for interlayer NN, NNN, and TNN displacements are denoted by $\Delta\theta_{NN}$, $\Delta\theta_{NNN}$, and $\Delta\theta_{TNN}$, respectively. The calculated interlayer hybridization strengths $\Delta\varepsilon_+$ (here labeled as $\Delta\varepsilon$) and $\Delta\varepsilon_-$ (i.e., $-\Delta\varepsilon$) in Eq. (34) decrease with the increasing energy ε.

$$[\phi^t]^\dagger U^\dagger \phi^b = \sum_{i=0}^{5} t_0(\boldsymbol{v}_0)\left(a_i^b a_i^{t\,*}\right) + t_1(\boldsymbol{v}_1)\left(a_0^b a_5^{t\,*} + a_1^b a_0^{t\,*} + a_2^b a_1^{t\,*} + a_3^b a_2^{t\,*} + a_4^b a_3^{t\,*} + a_5^b a_4^{t\,*}\right)$$
$$+ t_2(\boldsymbol{v}_2)\left(a_0^b a_1^{t\,*} + a_1^b a_2^{t\,*} + a_2^b a_3^{t\,*} + a_3^b a_4^{t\,*} + a_4^b a_5^{t\,*} + a_5^b a_0^{t\,*}\right). \tag{35}$$

Equations (28) and (32) have been used to obtain Eq. (35), which can be further rewritten as

$$[\phi^b]^\dagger U \phi^t = \sum_{j=0}^{5} t_0(\boldsymbol{v}_0)\left(a_{\boldsymbol{r}_j}^{b,*} a_{\boldsymbol{r}_j+\boldsymbol{v}_0}^t\right) + \sum_{j=0}^{5} t_1(\boldsymbol{v}_1)\left(a_{\boldsymbol{r}_j}^{b,*} a_{\boldsymbol{r}_j+\boldsymbol{v}_1}^t\right) + \sum_{j=0}^{5} t_2(\boldsymbol{v}_2)\left(a_{\boldsymbol{r}_j}^{b,*} a_{\boldsymbol{r}_j+\boldsymbol{v}_2}^t\right),$$
$$[\phi^t]^\dagger U^\dagger \phi^b = \sum_{j=0}^{5} t_0(\boldsymbol{v}_0)\left(a_{\boldsymbol{r}_j}^{b} a_{\boldsymbol{r}_j+\boldsymbol{v}_0}^{t,*}\right) + \sum_{j=0}^{5} t_1(\boldsymbol{v}_1)\left(a_{\boldsymbol{r}_j}^{b} a_{\boldsymbol{r}_j+\boldsymbol{v}_1}^{t,*}\right) + \sum_{j=0}^{5} t_2(\boldsymbol{v}_2)\left(a_{\boldsymbol{r}_j}^{b} a_{\boldsymbol{r}_j+\boldsymbol{v}_2}^{t,*}\right), \tag{36}$$

where $\boldsymbol{v}_0$, $\boldsymbol{v}_1$, and $\boldsymbol{v}_2$ are the interlayer NN, NNN, and TNN displacements. Equations (34) and (36) indicate that the interlayer hybridization strength $\Delta\varepsilon_-$ and $\Delta\varepsilon_+$ are determined by these interlayer hoppings $t_0(\boldsymbol{v}_0)$, $t_1(\boldsymbol{v}_1)$, and $t_2(\boldsymbol{v}_2)$ and the wave-function phase difference of pairing states for these NN, NNN, and TNN displacements. As shown in Fig. 10 and Eqs. (30) and (31), with the increasing energy, i.e., ϕ_i from ϕ_0 to ϕ_5, the absolute values $|\Delta\theta_{NN}^j|$ (with $e^{i\Delta\theta_{NN}^j} = a_{\boldsymbol{r}_j}^{b,*} a_{\boldsymbol{r}_j+\boldsymbol{v}_0}^t$) of phase differences $\Delta\theta_{NN}^j$ of each pairing states ϕ_i^b and ϕ_i^t for the interlayer NN displacements are always equal to 0, namely, $\Delta\theta_{NN} = 0$. For ϕ_i from ϕ_0 to ϕ_5, both the absolute values $|\Delta\theta_{NNN}^j|$ (with $e^{i\Delta\theta_{NNN}^j} = a_{\boldsymbol{r}_j}^{b,*} a_{\boldsymbol{r}_j+\boldsymbol{v}_1}^t$) and $|\Delta\theta_{TNN}^j|$ (with $e^{i\Delta\theta_{TNN}^j} = a_{\boldsymbol{r}_j}^{b,*} a_{\boldsymbol{r}_j+\boldsymbol{v}_2}^t$) of phase differences $\Delta\theta_{NNN}^j$ and $\Delta\theta_{TNN}^j$

for the interlayer NNN and TNN displacements vary in a form of

$$\left|\Delta\theta_{NNN}^j\right| = \left|\Delta\theta_{TNN}^j\right| = |\Delta\theta_{NNN}| = |\Delta\theta_{TNN}|$$
$$= 0 \to \pi/3 \to \pi/3 \to 2\pi/3 \to 2\pi/3 \to \pi. \tag{37}$$

Therefore, with the increasing energy from negative to positive values, the size $\Delta\varepsilon$ of the interlayer hybridization strength for the bonding and antibonding states (i.e., $\Delta\varepsilon = \Delta\varepsilon_+ = -\Delta\varepsilon_-$) vary with

$$\Delta\varepsilon = t_0(\boldsymbol{v}_0) + t_1(\boldsymbol{v}_1) + t_2(\boldsymbol{v}_2) \to t_0(\boldsymbol{v}_0) + \sqrt{3}[t_1(\boldsymbol{v}_1)$$
$$+ t_2(\boldsymbol{v}_2)]/2 \to t_0(\boldsymbol{v}_0) + \sqrt{3}[t_1(\boldsymbol{v}_1) + t_2(\boldsymbol{v}_2)]/2$$

$$\to t_0(\boldsymbol{\nu}_0) - [t_1(\boldsymbol{\nu}_1) + t_2(\boldsymbol{\nu}_2)]/2 \to t_0(\boldsymbol{\nu}_0) - [t_1(\boldsymbol{\nu}_1)$$
$$+ t_2(\boldsymbol{\nu}_2)]/2 \to t_0(\boldsymbol{\nu}_0) - t_1(\boldsymbol{\nu}_1) - t_2(\boldsymbol{\nu}_2). \tag{38}$$

Equation (38) indicates $t_1(\boldsymbol{\nu}_1)$, $t_2(\boldsymbol{\nu}_2)$, $\Delta\theta_{\text{NNN}}^j$, and $\Delta\theta_{\text{TNN}}^j$ are responsible for the electron-hole asymmetry of the interlayer hybridization with the stronger hybridization strength for holes in the structure of two six-carbon rings.

where $\sum_{i=0}^{N-1} |a_i^{b/t}|^2 = 1$. The hybridization states read as

$$\varphi_- = \frac{1}{\sqrt{2}}\begin{pmatrix} \phi^b \\ -\phi^t \end{pmatrix} = \frac{1}{\sqrt{2}}\left(a_0^b, a_1^b, \ldots, a_{N-1}^b, -a_0^t, -a_1^t, \ldots, -a_{N-1}^t\right)^T,$$

$$\varphi_+ = \frac{1}{\sqrt{2}}\begin{pmatrix} \phi^b \\ \phi^t \end{pmatrix} = \frac{1}{\sqrt{2}}\left(a_0^b, a_1^b, \ldots, a_{N-1}^b, a_0^t, a_1^t, \ldots, a_{N-1}^t\right)^T. \tag{40}$$

The interlayer hybridization strengths of the hybridization states $\varphi_\pm$ have the same forms as Eq. (34), where $[\phi^b]^\dagger U \phi^t$ and $[\phi^t]^\dagger U^\dagger \phi^b$ for the arbitrary BG system including $2N$ atoms can be written as

$$[\phi^b]^\dagger U \phi^t = \sum_{j=0}^{N-1}\sum_{\boldsymbol{\nu}_0} t_0(\boldsymbol{\nu}_0)\left(a_{\boldsymbol{r}_j}^{b,*} a_{\boldsymbol{r}_j+\boldsymbol{\nu}_0}^t\right) + \sum_{j=0}^{N-1}\sum_{\boldsymbol{\nu}_1} t_1(\boldsymbol{\nu}_1)\left(a_{\boldsymbol{r}_j}^{b,*} a_{\boldsymbol{r}_j+\boldsymbol{\nu}_1}^t\right) + \sum_{j=0}^{N-1}\sum_{\boldsymbol{\nu}_2} t_2(\boldsymbol{\nu}_2)\left(a_{\boldsymbol{r}_j}^{b,*} a_{\boldsymbol{r}_j+\boldsymbol{\nu}_2}^t\right),$$

$$[\phi^t]^\dagger U^\dagger \phi^b = \sum_{j=0}^{N-1}\sum_{\boldsymbol{\nu}_0} t_0(\boldsymbol{\nu}_0)\left(a_{\boldsymbol{r}_j}^b a_{\boldsymbol{r}_j+\boldsymbol{\nu}_0}^{t,*}\right) + \sum_{j=0}^{N-1}\sum_{\boldsymbol{\nu}_1} t_1(\boldsymbol{\nu}_1)\left(a_{\boldsymbol{r}_j}^b a_{\boldsymbol{r}_j+\boldsymbol{\nu}_1}^{t,*}\right) + \sum_{j=0}^{N-1}\sum_{\boldsymbol{\nu}_2} t_2(\boldsymbol{\nu}_2)\left(a_{\boldsymbol{r}_j}^b a_{\boldsymbol{r}_j+\boldsymbol{\nu}_2}^{t,*}\right). \tag{41}$$

The pairing states $\phi^{b/t}$ are the same for equivalent and mixed hybridizations according to the hybridization selection rules in Table V, and hence the interlayer NN phase difference $\Delta\theta_{\text{NN}}^j$ is always 0, i.e., $a_{\boldsymbol{r}_j}^{b,*} a_{\boldsymbol{r}_j+\boldsymbol{\nu}_0}^t = 1$, in Eq. (41). As a result, with the increasing energy, the hybridization strength $\Delta\varepsilon$ is changed by the interlayer non-nearest-neighbor hoppings t_1 and t_2 and phase differences $\Delta\theta_{\text{NNN}}^j$ (with $e^{i\Delta\theta_{\text{NNN}}^j} = a_{\boldsymbol{r}_j}^{b,*} a_{\boldsymbol{r}_j+\boldsymbol{\nu}_1}^t$) and $\Delta\theta_{\text{TNN}}^j$ (with $e^{i\Delta\theta_{\text{TNN}}^j} = a_{\boldsymbol{r}_j}^{b,*} a_{\boldsymbol{r}_j+\boldsymbol{\nu}_2}^t$). Different from the simplest case of twisted two-six carbon rings, for the twisted BG with a large number of carbon atoms, the energy of the state φ_- can be lower or higher than the energy of state φ_+ depending on the pairing states, and thus φ_- and φ_+ do not correspond to the bonding and antibonding states.

For nonequivalent hybridizations in D_{6d} graphene quasicrystal systems in Eq. (8), $\phi_{B_i}^b$ and $\phi_{B_i}^t$ with irrep B_i have the same energy $\varepsilon_{B_i}^b = \varepsilon_{B_i}^t$ with $i = 1, 2$, after the local reflection

Let us discuss an arbitrary BG system including $2N$ atoms with N as the number of atoms in one monolayer. The interlayer NN hopping $t_0(\boldsymbol{\nu}_0)$, NNN hopping $t_1(\boldsymbol{\nu}_1)$, and TNN hopping $t_2(\boldsymbol{\nu}_2)$ are determined by Eqs. (C1) and (C2). The pairing states $\phi^{b/t}$ are written as

$$\phi^{b/t} = \left(a_0^{b/t}, a_1^{b/t}, \ldots, a_{N-1}^{b/t}\right)^T, \tag{39}$$

plane is chosen, i.e., $\sigma_{v,0}^b = \sigma_x$ and $\sigma_{v,i}^t = \sigma_{d,i}^b$. Consequently, two nonequivalent hybridizations $B_1^b + B_2^t$ and $B_2^b + B_1^t$ in Eq. (8) with sign $+$ denoting pairing are actually the same, and hence we can perform a following transformation of the wave functions of two nonequivalent hybridizations to obtain a uniform expression of the pairing states

$$\begin{pmatrix} \phi_+^{b/t} \\ \phi_-^{b/t} \end{pmatrix} = \frac{1}{\sqrt{2}}\begin{pmatrix} 1 & 1 \\ 1 & -1 \end{pmatrix}\begin{pmatrix} \phi_{B_1}^{b/t} \\ \phi_{B_2}^{b/t} \end{pmatrix}, \tag{42}$$

where the pairing states $\phi_\lambda^{b/t}$ with $\lambda = +$ or $-$ are written as

$$\phi_\lambda^{b/t} = \left(c_{\lambda,0}^{b/t}, c_{\lambda,1}^{b/t}, \ldots, c_{\lambda,N-1}^{b/t}\right)^T, \tag{43}$$

with $\sum_{i=0}^{N-1} |c_{\lambda,i}^{b/t}|^2 = 1$. The hybridization states read as

$$\varphi_{\lambda,-} = \frac{1}{\sqrt{2}}\begin{pmatrix} \phi_\lambda^b \\ -\phi_\lambda^t \end{pmatrix} = \frac{1}{\sqrt{2}}\left(c_{\lambda,0}^b, c_{\lambda,1}^b, \ldots, c_{\lambda,N-1}^b, -c_{\lambda,0}^t, -c_{\lambda,1}^t, \ldots, -c_{\lambda,N-1}^t\right)^T,$$

$$\varphi_{\lambda,+} = \frac{1}{\sqrt{2}}\begin{pmatrix} \phi_\lambda^b \\ \phi_\lambda^t \end{pmatrix} = \frac{1}{\sqrt{2}}\left(c_{\lambda,0}^b, c_{\lambda,1}^b, \ldots, c_{\lambda,N-1}^b, c_{\lambda,0}^t, c_{\lambda,1}^t, \ldots, c_{\lambda,N-1}^t\right)^T. \tag{44}$$

The interlayer hybridization strengths of the hybridization states have the same forms as Eq. (34), where $[\phi_\lambda^b]^\dagger U \phi_\lambda^t$ and $[\phi_\lambda^t]^\dagger U^\dagger \phi_\lambda^b$ for the arbitrary BG system including $2N$ atoms can be written as

$$[\phi_\lambda^b]^\dagger U \phi_\lambda^t = \sum_{j=0}^{N-1}\sum_{\boldsymbol{\nu}_0} t_0(\boldsymbol{\nu}_0)\left(c_{\lambda,\boldsymbol{r}_j}^{b,*} c_{\lambda,\boldsymbol{r}_j+\boldsymbol{\nu}_0}^t\right) + \sum_{j=0}^{N-1}\sum_{\boldsymbol{\nu}_1} t_1(\boldsymbol{\nu}_1)\left(c_{\lambda,\boldsymbol{r}_j}^{b,*} c_{\lambda,\boldsymbol{r}_j+\boldsymbol{\nu}_1}^t\right) + \sum_{j=0}^{N-1}\sum_{\boldsymbol{\nu}_2} t_2(\boldsymbol{\nu}_2)\left(c_{\lambda,\boldsymbol{r}_j}^{b,*} c_{\lambda,\boldsymbol{r}_j+\boldsymbol{\nu}_2}^t\right),$$

$$[\phi_\lambda^t]^\dagger U^\dagger \phi_\lambda^b = \sum_{j=0}^{N-1}\sum_{\boldsymbol{\nu}_0} t_0(\boldsymbol{\nu}_0)\left(c_{\lambda,\boldsymbol{r}_j}^b c_{\lambda,\boldsymbol{r}_j+\boldsymbol{\nu}_0}^{t,*}\right) + \sum_{j=0}^{N-1}\sum_{\boldsymbol{\nu}_1} t_1(\boldsymbol{\nu}_1)\left(c_{\lambda,\boldsymbol{r}_j}^b c_{\lambda,\boldsymbol{r}_j+\boldsymbol{\nu}_1}^{t,*}\right) + \sum_{j=0}^{N-1}\sum_{\boldsymbol{\nu}_2} t_2(\boldsymbol{\nu}_2)\left(c_{\lambda,\boldsymbol{r}_j}^b c_{\lambda,\boldsymbol{r}_j+\boldsymbol{\nu}_2}^{t,*}\right). \tag{45}$$
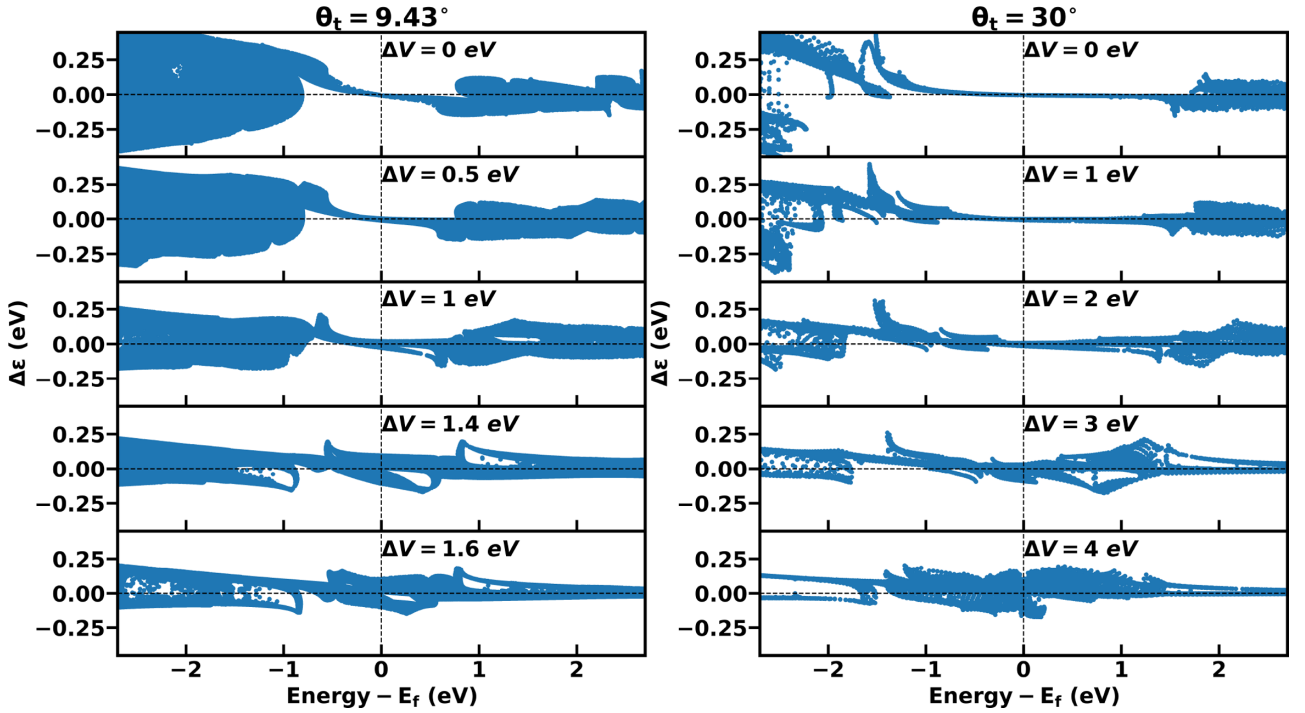
FIG. 11. The hybridization strengths under different interlayer potential difference $\triangle V$ as a function of energy for twisted BG with $\theta_t = 9.43°$ (left panel) and graphene quasicrystal simulated by a periodic 15/26 approximant (right panel).

In this respect, for the same λ, ϕ_λ^b and ϕ_λ^t are the same, and hence the interlayer NN phase difference $\Delta\theta_{\text{NN}}^j$ is also 0, i.e., $c_{\lambda,\boldsymbol{r}_j}^{b,*} c_{\lambda,\boldsymbol{r}_j+\boldsymbol{v}_0}^t = 1$. As a result, with the increasing energy, the hybridization strength $\Delta\varepsilon$ is still changed by the interlayer non-nearest-neighbor hoppings t_1 and t_2 and the phase differences $\Delta\theta_{\text{NNN}}^j$ (with $e^{i\Delta\theta_{\text{NNN}}^j} = c_{\lambda,\boldsymbol{r}_j}^{b,*} c_{\lambda,\boldsymbol{r}_j+\boldsymbol{v}_1}^t$) and $\Delta\theta_{\text{TNN}}^j$ (with $e^{i\Delta\theta_{\text{TNN}}^j} = c_{\lambda,\boldsymbol{r}_j}^{b,*} c_{\lambda,\boldsymbol{r}_j+\boldsymbol{v}_2}^t$) of the pairing states $\phi_\lambda^{b/t}$. In a word, for three categories of hybridizations in Table V, with the increasing energy, the electron-hole asymmetrical hybridization with the stronger hybridization strength for holes is a result of non-nearest-neighbor interlayer hoppings and phase differences of pairing states.

C. Electric field effects on hybridization strength

The interlayer potential difference $\triangle V$ induced by a vertical electric field is usually applied to modify the electronic structures and transport properties of twisted BG to achieve gate-controllable devices. Here we reveal the electric field effects on the hybridization strength in twisted BGs. Figure 11 shows the hybridization strengths under different interlayer potential difference $\triangle V$ in twisted BG with $\theta_t = 9.43°$ and graphene quasicrystal simulated by a periodic 15/26 approximant. With the increasing interlayer potential difference $\triangle V$, the hybridization strengths near the Fermi level are enhanced. The results can be still explained by the second-order nondegenerate perturbation theory at nondegenerate energy positions and the first-order degenerate perturbation theory at degenerate energy positions. For example, for the unfolded band structures of twisted BG with $\theta_t = 9.43°$ in Fig. 12, the

interlayer potential difference $\triangle V$ lifts the Dirac linear dispersion around K^b of the bottom layer and moves down the Dirac linear dispersion around K^t of the top layer. Consequently, the energy difference between the two linear bands is reduced near the Fermi level, and hence the hybridization strength is enhanced near the Fermi level according to the second-order nondegenerate perturbation theory. For the degenerate energy positions, the first-order degenerate perturbation theory induces an obvious hybridization strength as well.

D. Electric field effects on resonant quasicrystalline states

Due to the quasiperiodicity, there are resonant quasicrystalline states in graphene quasicrystal, which originate from the resonant coupling of the Bloch functions with the same energy. The $\boldsymbol{k}$ points of these Bloch functions are plotted in Fig. 13. Among the 12 $\boldsymbol{k}$ points, 6 $\boldsymbol{k}$ points belong to the bottom layer with $\boldsymbol{k}^b = \boldsymbol{k}_0 + \boldsymbol{G}^t$ and 6 $\boldsymbol{k}$ points belong to the top layer with $\boldsymbol{k}^t = \boldsymbol{k}_0 + \boldsymbol{G}^b$, where $\boldsymbol{k}_0 = 0$ and $\boldsymbol{G}^b$ and $\boldsymbol{G}^t$ are the reciprocal points of the bottom and top layers with $|\boldsymbol{G}^b| = |\boldsymbol{G}^t| = 4\pi/\sqrt{3}a$. It can be easily checked that any $\boldsymbol{k}^b$ and $\boldsymbol{k}^t$ satisfy the wave-vector-dependent interlayer coupling condition in Eqs. (23) and (24). The 12 $\boldsymbol{k}$ points are made up of two C_{6v} subsystems of the six $\boldsymbol{k}$ points denoted by black empty dots from the bottom layer and the six $\boldsymbol{k}$ points denoted by red solid dots from the top layer in Fig. 13 and the Hamiltonian keeps the D_{6d} point-group symmetry including the operations

$$E = I(12) \otimes \sigma_0,$$
$$S_{12}^{2i+1} = S_{12}^{2i+1}(\boldsymbol{k}) \otimes \sigma_0 \quad (i = 0, 1, \dots, 5),$$
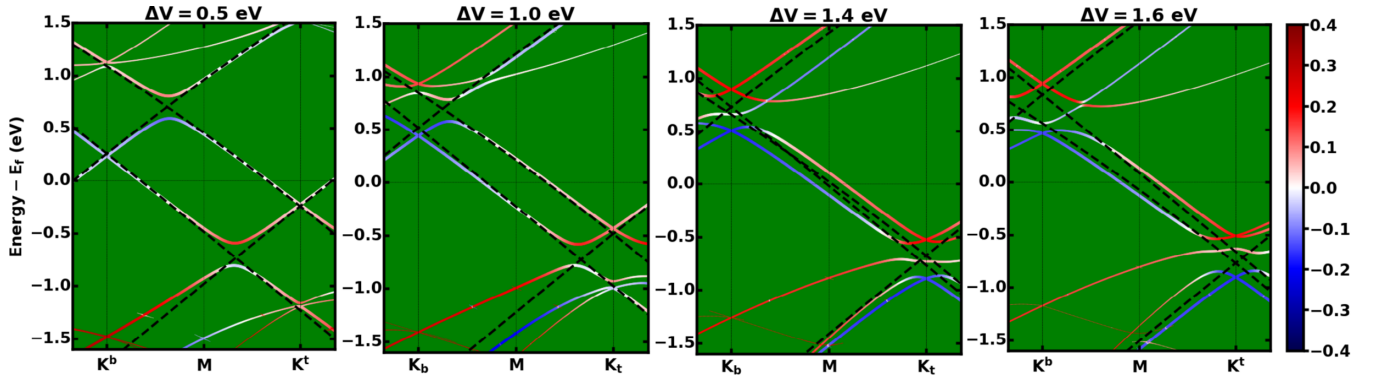$$C_{12}^{2i} = C_{12}^{2i}(\boldsymbol{k}) \otimes \sigma_0 \quad (i = 1, 2, \dots, 5),$$

FIG. 12. The calculated unfolded band structures for twisted BG with $\theta_t = 9.43°$ under different interlayer potential difference $\triangle V$, where the color map denotes the interlayer hybridization strength $\triangle \varepsilon$, and black dashed lines stand for the band structures of the bottom and top graphene monolayers.

$$C'_{2,i} = C'_{2,i}(\boldsymbol{k}) \otimes \sigma_1 \quad (i = 0, 1, \ldots, 5),$$
$$\sigma_{d,i} = \sigma_{d,i}(\boldsymbol{k}) \otimes \sigma_1 \quad (i = 0, 1, \ldots, 5), \quad (46)$$

where $I(12)$, $S_{12}^{2i+1}(\boldsymbol{k})$, $C_{12}^{2i}(\boldsymbol{k})$, $C'_{2,i}(\boldsymbol{k})$, and $\sigma_{d,i}(\boldsymbol{k})$ are the symmetry operations acting on the 12 $\boldsymbol{k}$ points, and σ_0 and σ_1 are the identity operation $I(2)$ and the x component of Pauli matrices, respectively, acting on the sublattice. In the direct product space of the $\boldsymbol{k}$ space and sublattice space, one can construct a 24×24 tight-binding Hamiltonian for the resonant quasicyrstalline states [27]

$$H = \begin{pmatrix} H^{(0)} & W_{0,1} & & & & W_{11,0}^\dagger \\ W_{0,1}^\dagger & H^{(1)} & W_{1,2} & & & \\ & W_{1,2}^\dagger & H^{(2)} & \ddots & & \\ & & \ddots & \ddots & W_{9,10} & \\ & & & W_{9,10}^\dagger & H^{(10)} & W_{10,11} \\ W_{11,0} & & & & W_{10,11}^\dagger & H^{(11)} \end{pmatrix}.$$
$$(47)$$
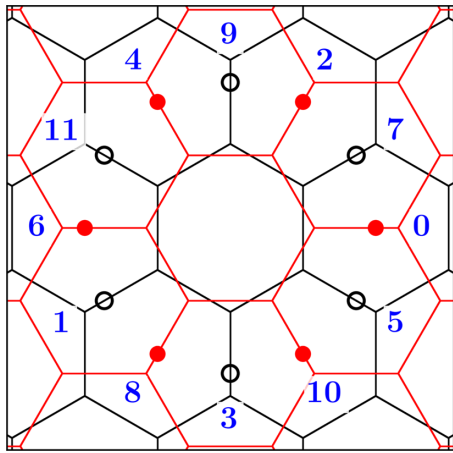

FIG. 13. The 12 k points for constructing the 24×24 Hamiltonian of the resonant states in reciprocal space. The black and red hexagon networks, respectively, denote the Brillouin zones for the bottom and top layers. The 12 k points are labeled by black empty and red solid dots with corresponding numbers from the two C_{6v} subsystems.

Here, $H^{(n)}$ is the Hamiltonian at nth k point with the form

$$H^{(n)} = \begin{pmatrix} \Delta V/2 & 0.682\gamma_0 \\ 0.682\gamma_0 & \Delta V/2 \end{pmatrix} \quad \text{(odd n)},$$
$$H^{(n)} = \begin{pmatrix} -\Delta V/2 & 0.682\gamma_0 \\ 0.682\gamma_0 & -\Delta V/2 \end{pmatrix} \quad \text{(even n)},$$
$$(48)$$

where ΔV is the interlayer potential difference induced by the vertical electric field. $W_{n,n+1}$ is the interlayer interaction between nth and $(n + 1)$th k points. If the sublattice order is rearranged as (A^b, B^b) or (A^t, B^t) when $n \mod 4 = 2, 3$ and (B^b, A^b) or (B^t, A^t) when $n \mod 4 = 0, 1$, all of the interlayer interaction matrices $W_{n,n+1}$'s have the same form

$$W_{n,n+1} = T_0 \begin{pmatrix} e^{\frac{2\pi}{3}i} & 1 \\ 1 & e^{-\frac{2\pi}{3}i} \end{pmatrix}, \quad (49)$$

where T_0 is 0.157 eV according to the tight-binding parameters (see Appendix C). The rearrangement of the sublattice order has no influence on $H^{(n)}$.

For each isolated C_{6v} subsystem, the energy gap is 3.68 eV because of the intralayer sublattice interaction, as denoted by the energy difference between the positive and negative energy levels with black lines in Fig. 14(a). The energy of the hybridization states is denoted by the red lines. The interlayer hybridizations follow the selection rule in Eqs. (7) and (8) and the hybridization strength $\Delta \varepsilon$ for the valence band is stronger than that for the conduction band. As shown by the insets in Fig. 14(a), the hybridization states from the equivalent hybridizations are 12-fold symmetrical. The nonequivalent hybridizations $B_1 + B_2 \Rightarrow E_3 + E_3$ and $B_2 + B_1 \Rightarrow E_3 + E_3$ are quite weak because of the large energy difference of about 3.68 eV, and all of the E_3 states are sixfold symmetrical.

If a vertical electric field is applied, an additional interlayer potential difference ΔV should be taken into account. In this respect, the D_{6d} symmetry of the bilayer system is broken into C_{6v}. The previous E_4 and E_5 states in D_{6d} point group formed by the equivalent hybridizations become E_2 and E_1 states in C_{6v} point group, and the E_3 states from the nonequivalent hybridizations become B_1 and B_2 states, as shown in Figs. 14(b) and 14(c). The hybridization states from the equivalent hybridizations will also lose the 12-fold symmetry. With the increasing ΔV from 0 to 3.68 eV, the hybridizations of $A_1 + A_1$, $A_2 + A_2$, and $B_1 + B_2$ weaken much because of the
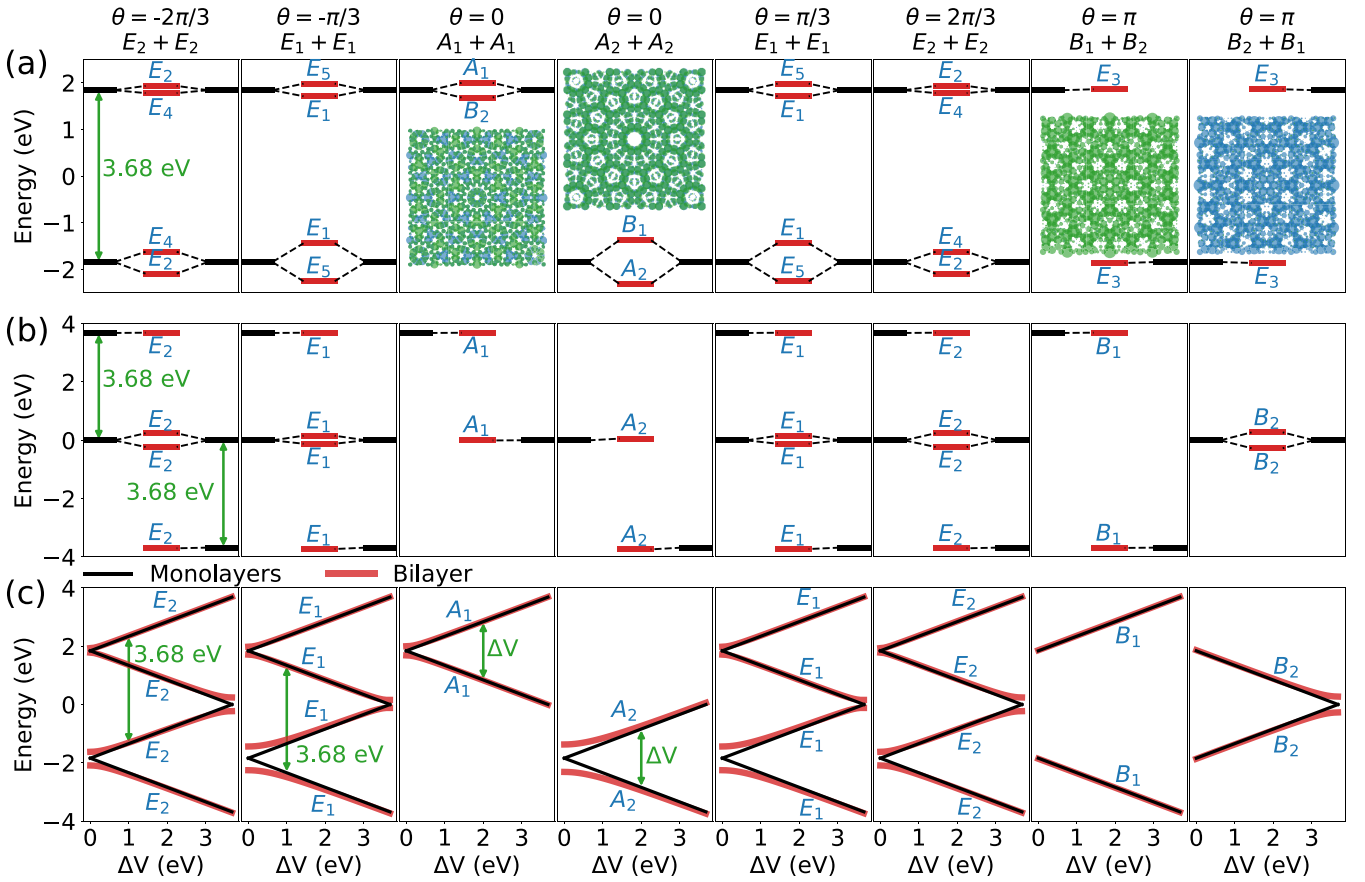
FIG. 14. The eigenenergy spectrum and their irreps of the 12 k-points model in reciprocal space with respect to C_6 for (a) $\Delta V = 0$ eV, and (b) $\Delta V = 3.68$ eV. The left and right black lines in each subplot denote the pairing states from two C_{6v} subsystems, and the middle red lines denote the hybridization states for D_{6d} bilayer. The insets show the real-space electron density for the bonding B_2 state, the antibonding B_1 state, and two bonding E_3 states in corresponding subplots. (c) The energy levels of the pairing and hybridization states as a function of ΔV.

enlarged energy difference, and the hybridizations of $B_2 + B_1$, $E_1 + E_1$, and $E_2 + E_2$ weaken slightly at first and then strengthen, as shown in Fig. 14(c). Therefore, the electric field acts as a polarizer, which filters the hybridizations of $A_1 + A_1$, $A_2 + A_2$, and $B_1 + B_2$ and allows the hybridizations of $B_2 + B_1$, $E_1 + E_1$, and $E_2 + E_2$.

VII. PROPOSALS IDENTIFYING BAND STRUCTURES EXPERIMENTALLY

Figure 15(a) shows the unfolded energy band structures of graphene quasicrystal with a supercell of the periodic 15/26 approximant along the same k path of the primitive unit cell of graphene. The dot lines with the dot size as the value of spectral weight (i.e., $p_{n'k} = \sum_{n,s} |\langle \phi_{nk}^s | \varphi_{n'k} \rangle|^2$ [33]) represent the unfolded band structures, where $\varphi_{n'k}$ is the eigenstate of the quasicrystal with the band index n' and wave vector k, and ϕ_{nk}^s is the eigenstate of graphene with the band index n and the layer index s. The color of the dot line represents the interlayer hybridization strength $\Delta\varepsilon$ in Eq. (18). We see again the two hybridization characteristics in graphene quasicrystal: (i) the weak hybridization strength inside low-energy area and (ii) the electron-hole asymmetrical hybridization inside high-energy areas. Optical conductivity with its real part corresponding to the optical absorption man-

ifests the interband transitions as a result of optical selection rule [45], and hence is employed to determine the allowed transitions of energy states with their symmetry properties. By using the TB propagation method combined with the Kubo-Greenwood formula (see Appendix F), the real part of optical conductivity as a function of photon energy $\hbar\omega$ is calculated and shown in Figs. 15(b)–15(d) at $\mu = 0$, -1.9, and 1.67 eV, respectively, where the chemical potential μ can be tuned by a gate voltage. In Fig. 15(b) at $\mu = 0$ eV, the optical conductivity of quasicrystal is almost the same as that of graphene for about $\hbar\omega < 2.5$ eV, which indicates the weak hybridization inside the low-energy area. In Figs. 15(c) and 15(d) with $\mu = -1.9$ and 1.67 eV, respectively, the optical conductivity spectra show remarkably different energy positions of absorption peaks, which arise from the interband transitions between these hybridization states in negative and positive high-energy areas, respectively. The zoomed-in images of unfolded band structures and corresponding optical conductivity spectra in Fig. 15 are plotted in Fig. 16. The irreps of bands at Q point are obtained and labeled near $\mu = -1.9$ and 1.67 eV, respectively. The optical selection rules of D_{6d} point group read as [45] $A_1 \leftrightarrow E_1$, $A_2 \leftrightarrow E_1$, $B_1 \leftrightarrow E_5$, $B_2 \leftrightarrow E_5$, $E_1 \leftrightarrow E_2$, $E_2 \leftrightarrow E_3$, $E_3 \leftrightarrow E_4$, and $E_4 \leftrightarrow E_5$. Following the optical selection rules, the allowed transitions at $\mu = 1.67$ eV in Fig. 16(a) corresponding to the absorption
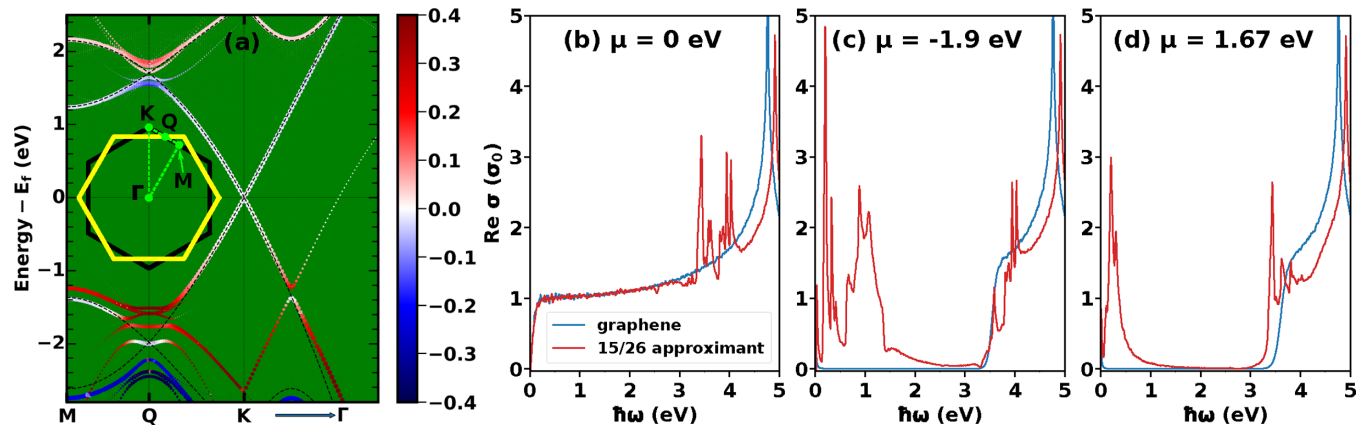
FIG. 15. (a) The calculated unfolded band structures for dodecagonal graphene quasicrystal within a periodic 15/26 approximant, where the color map denotes the interlayer hybridization strength $\triangle \varepsilon$, and black dashed lines stand for the band structures of the bottom and top graphene monolayers. The real part of optical conductivity as a function of photon energy $\hbar\omega$ at $\mu = 0$ eV in (b), $\mu = -1.9$ eV in (c), and $\mu = 1.67$ eV in (d), where the red and blue lines are for quasicrystal and graphene monolayer, respectively. The optical conductivity is in units of $\sigma_0 = \frac{\pi e^2}{2h}$.

peaks are $E_4 \leftrightarrow E_3$ for peak 1, $E_4 \leftrightarrow E_5$ for peak 2, and both $E_1 \leftrightarrow A_1$ and $B_2 \leftrightarrow E_5$ for peak 3 in Fig. 16(b). The allowed transitions at $\mu = -1.9$ eV in Fig. 16(c) corresponding to the absorption peaks are $E_3 \leftrightarrow E_4$ for peaks 1, 2, and 3 because of the special profiles of E_3 and E_4 bands and the splitting of E_4 band, both $E_2 \leftrightarrow E_1$ and $E_5 \leftrightarrow E_4$ for peak 4, and both $E_5 \leftrightarrow B_1$ and $A_2 \leftrightarrow E_1$ for peak 5, and $A_2 \leftrightarrow E_1$ for peak 6

because of the special profiles and splitting of E_1 band in Fig. 16(d). Thus, the electron-hole asymmetrical hybridization can be characterized by optical conductivity spectrum experimentally. On the other hand, these hybridization-generated band structures with their hybridization strengths in graphene quasicrystal can also be measured by ARPES [17,18].
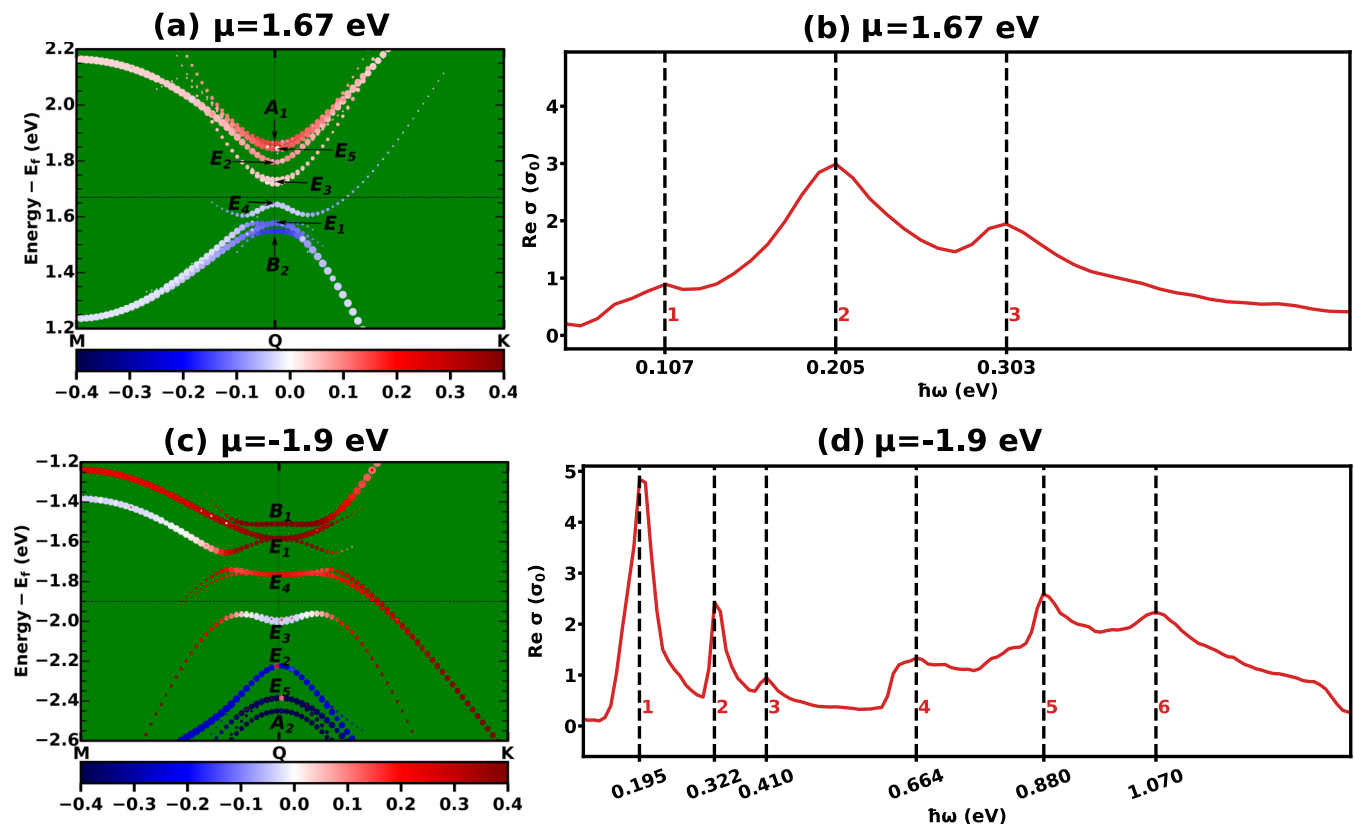

FIG. 16. The zoomed-in images of unfolded band structures of Fig. 15 (a) near $\mu = 1.67$ eV in (a) and near $\mu = -1.9$ eV in (c) and corresponding zoomed-in optical conductivity spectra here in (b) and (d), respectively.

VIII. CONCLUSION

The constructed hybridization rules and classifications together with numerical results indicate that the D_{6h} untwisted BG only allows equivalent hybridization, the D_6 twisted BG allows equivalent and mixed hybridizations, and the D_{6d} graphene quasicrystalline permits equivalent and nonequivalent hybridizations. The large energy difference between Dirac bands from top and bottom layers renders a weak hybridization strength near the Fermi level in twisted BG systems. The non-nearest-neighbor interlayer hoppings and the wave-function phase difference between pairing states enable the electron-hole asymmetry of hybridization strength. The calculated optical conductivity spectra in graphene quasicrystalline manifest the hybridization strength characteristics. Our results deeply explore how the interlayer states couple with each other in these BG systems and shed light on the extrinsic quasicrystals in van der Waals layered structures. In view of the successful experimental synthesis of graphene quasicrystal [17–25] and the state-of-art fabrication technology of graphene-based nanostructures [46–48], we expect that the hybridization selection rules and the electron-hole asymmetrical hybridization effect are verified experimentally by optical absorption spectrum and ARPES.

APPENDIX A: DERIVATION OF INTERLAYER HYBRIDIZATION SELECTION RULES

1. D_{6d} graphene quasicrystals

The incommensurate $30°$ twisted BG has D_{6d} point-group symmetry in Table II. Due to the $30°$ twist angle, the mirror reflections of the two layers have the relationships of $\sigma_{v,i}^t = \sigma_{d,i}^b$ and $\sigma_{d,i}^t = \sigma_{v,j}^b$ with $j = (i+1) \bmod 3$, where $i, j = 0, 1, 2$. From the character table of C_{6v} in Table I, one can find that the projection operators of the two layers have the following properties:

(i) For irrep $ir \in \{A_1, A_2, E_1, E_2\}$, the same characters for $\sigma_{v,i}$ and $\sigma_{d,i}$ enable

$$P_{ir}^{C_{6v}^b} = P_{ir}^{C_{6v}^t}. \tag{A1}$$

(ii) For irreps B_1 and B_2, the opposite characters for $\sigma_{v,i}$ and $\sigma_{d,i}$ enable

$$P_{B_1}^{C_{6v}^b} = P_{B_2}^{C_{6v}^t}, \quad P_{B_2}^{C_{6v}^b} = P_{B_1}^{C_{6v}^t}. \tag{A2}$$

(iii) For irrep $ir \in \{A_1, A_2, B_1, B_2, E_1, E_2\}$, because the characters of all operations are real numbers and an arbitrary symmetry operation and its inverse operation are inside the

TABLE VI. Character table of C_6. $\varepsilon = e^{\frac{\pi i}{3}}$.

C_6	E	C_6	C_3	C_2	C_3^2	$3C_6^5$
A	1	1	1	1	1	1
B	1	-1	1	-1	1	-1
E_1	1	ε	$-\varepsilon^*$	-1	$-\varepsilon$	ε^*
	1	ε^*	$-\varepsilon$	-1	$-\varepsilon^*$	ε
E_2	1	$-\varepsilon^*$	$-\varepsilon$	1	$-\varepsilon^*$	$-\varepsilon$
	1	$-\varepsilon$	$-\varepsilon^*$	1	$-\varepsilon$	$-\varepsilon^*$

same class, the projection operators satisfy

$$\left[P_{ir}^{C_{6v}^b}\right]^\dagger = P_{ir}^{C_{6v}^b}, \quad \left[P_{ir}^{C_{6v}^t}\right]^\dagger = P_{ir}^{C_{6v}^t}. \tag{A3}$$

(iv) For irrep $ir \in \{A_1, A_2, B_1, B_2, E_1, E_2\}$, because C_{6v} is a subgroup of D_{6d}, and hence all symmetry operations in C_{6v} commute with the Hamiltonian H, i.e,

$$\left[P_{ir}^{C_{6v}^b}, H\right] = \left[P_{ir}^{C_{6v}^t}, H\right] = 0. \tag{A4}$$

Using Eqs. (A1), (A3) and (A4) for irrep $ir \in \{A_1, A_2, E_1, E_2\}$, we write the hybridization matrix element $U_{ir,ir'}$ as

$$\begin{aligned} U_{ir,ir'} &= \left\langle \varphi_{ir}^b \middle| H \middle| \varphi_{ir'}^t \right\rangle = \left\langle \varphi_{ir}^b \middle| P_{ir}^{C_{6v}^b} H \middle| \varphi_{ir'}^t \right\rangle \\ &= \left\langle \varphi_{ir}^b \middle| H P_{ir}^{C_{6v}^b} \middle| \varphi_{ir'}^t \right\rangle = \left\langle \varphi_{ir}^b \middle| H P_{ir}^{C_{6v}^t} \middle| \varphi_{ir'}^t \right\rangle \\ &= \delta_{ir,ir'} U_{ir,ir'}. \end{aligned} \tag{A5}$$

Using Eqs. (A2)–(A4) for irreps B_1 and B_2, we write the hybridization matrix elements as

$$\begin{aligned} U_{B_1,ir'} &= \left\langle \varphi_{B_1}^b \middle| H \middle| \varphi_{ir'}^t \right\rangle = \left\langle \varphi_{B_1}^b \middle| P_{B_1}^{C_{6v}^b} H \middle| \varphi_{ir'}^t \right\rangle \\ &= \left\langle \varphi_{ir}^b \middle| H P_{B_1}^{C_{6v}^b} \middle| \varphi_{ir'}^t \right\rangle = \left\langle \varphi_{ir}^b \middle| H P_{B_2}^{C_{6v}^t} \middle| \varphi_{ir'}^t \right\rangle \\ &= \delta_{B_2,ir'} U_{B_1,ir'}, \end{aligned} \tag{A6}$$

and

$$\begin{aligned} U_{B_2,ir'} &= \left\langle \varphi_{B_2}^b \middle| H \middle| \varphi_{ir'}^t \right\rangle = \left\langle \varphi_{B_2}^b \middle| P_{B_2}^{C_{6v}^b} H \middle| \varphi_{ir'}^t \right\rangle \\ &= \left\langle \varphi_{ir}^b \middle| H P_{B_2}^{C_{6v}^b} \middle| \varphi_{ir'}^t \right\rangle = \left\langle \varphi_{ir}^b \middle| H P_{B_1}^{C_{6v}^t} \middle| \varphi_{ir'}^t \right\rangle \\ &= \delta_{B_1,ir'} U_{B_2,ir'}. \end{aligned} \tag{A7}$$

The constraint equations of the hybridization matrix elements in Eqs. (A5)–(A7) endow hybridization rules for these states from the top and bottom layers, i.e., the hybridization selection rule in D_{6d} graphene quasicrystal.

2. D_6 twisted BG with $0° < \theta_t < 30°$

The twisted BG with $0° < \theta_t < 30°$ has D_6 point-group symmetry in Table III. The intersection between C_{6v} and D_6 is C_6. From the character tables of C_{6v} in Table I and C_6 in Table VI, one can find that, for 1D irrep X_i with $i = 1, 2$ and $X = A$ or B,

$$\begin{aligned} P_A^{C_6} \left| \varphi_{X_i}^{b/t} \right\rangle &= \frac{1}{6} \sum_{i=0}^5 C_6^i \left| \varphi_{X_i}^{b/t} \right\rangle = \delta_{A,X} \left| \varphi_{X_i}^{b/t} \right\rangle \\ &= (\delta_{A_1,X_i} + \delta_{A_2,X_i}) \left| \varphi_{X_i}^{b/t} \right\rangle, \end{aligned}$$

$$P_B^{C_6} \left| \varphi_{X_i}^{b/t} \right\rangle = \frac{1}{6} \sum_{i=0}^{5} (-1)^i C_6^i \left| \varphi_{B_i}^{b/t} \right\rangle = \delta_{B,X} \left| \varphi_{X_i}^{b/t} \right\rangle$$
$$= (\delta_{B_1,X_i} + \delta_{B_2,X_i}) \left| \varphi_{X_i}^{b/t} \right\rangle. \tag{A8}$$

Because C_6 is a subgroup of D_6, all symmetry operations in C_6 commute with the Hamiltonian H, and hence the projection operators $P_A^{C_6}$ and $P_B^{C_6}$ also commute with H, i.e.,

$$\left[P_A^{C_6}, H \right] = \left[P_B^{C_6}, H \right] = 0. \tag{A9}$$

In addition, from the character tables of C_6, one can also find that

$$\left[P_A^{C_6} \right]^\dagger = P_A^{C_6}, \quad \left[P_B^{C_6} \right]^\dagger = P_B^{C_6}. \tag{A10}$$

Using Eqs. (A8)–(A10), we write the hybridization matrix elements for 1D irreps X_i with $X = A$ or B as

$$U_{A_i,X_j} = \left\langle \varphi_{A_i}^b \left| H \right| \varphi_{X_j}^t \right\rangle = \left\langle \varphi_{A_i}^b \left| P_A^{C_6} H \right| \varphi_{X_j}^t \right\rangle$$
$$= \left\langle \varphi_{A_i}^b \left| H P_A^{C_6} \right| \varphi_{X_j}^t \right\rangle = \delta_{A,X} U_{A_i,X_j}$$
$$= (\delta_{A_1,X_i} + \delta_{A_2,X_i}) U_{A_i,X_j},$$

$$U_{B_i,X_j} = \left\langle \varphi_{B_i}^b \left| H \right| \varphi_{X_j}^t \right\rangle = \left\langle \varphi_{B_i}^b \left| P_B^{C_6} H \right| \varphi_{X_j}^t \right\rangle$$
$$= \left\langle \varphi_{B_i}^b \left| H P_B^{C_6} \right| \varphi_{X_j}^t \right\rangle = \delta_{B,X} U_{B_i,X_j}$$
$$= (\delta_{B_1,X_i} + \delta_{B_2,X_i}) U_{B_i,X_j}. \tag{A11}$$

For 2D irreps E_i with $i = 1, 2$, because all the characters of the operation classes σ_v and σ_d in C_{6v} and the operation classes C_2' and C_2'' in D_6 are 0, the projection operators for irreps E_i in C_{6v} and D_6 have the following properties:

$$P_{E_i}^{C_{6v}^b} = P_{E_i}^{C_{6v}^t} = P_{E_i}^{D_6},$$
$$\left[P_{E_i}^{C_{6v}^b} \right]^\dagger = P_{E_i}^{C_{6v}^b} = \left[P_{E_i}^{C_{6v}^t} \right]^\dagger = P_{E_i}^{C_{6v}^t},$$
$$\left[P_{E_i}^{C_{6v}^b}, H \right] = \left[P_{E_i}^{C_{6v}^t}, H \right] = 0. \tag{A12}$$

Using Eq. (A12) we write the hybridization matrix elements for 2D irreps E_i as

$$U_{E_i,E_j} = \left\langle \varphi_{E_i}^b \left| H \right| \varphi_{E_j}^t \right\rangle = \left\langle \varphi_{E_i}^b \left| P_{E_i}^{C_{6v}^b} H \right| \varphi_{E_j}^t \right\rangle$$
$$= \left\langle \varphi_{E_i}^b \left| H P_{E_i}^{C_{6v}^t} \right| \varphi_{E_j}^t \right\rangle = \delta_{E_i,E_j} U_{E_i,E_j}. \tag{A13}$$

The constraint equations of the hybridization matrix elements in Eqs. (A11) and (A13) endow hybridization rules for these states from the top and bottom layers, i.e., the hybridization selection rules in D_6 twisted BGs.

3. D_{6h} untwisted BG

The untwisted AA-stacked BG with $\theta_t = 0°$ has D_{6h} point-group symmetry in Table IV. The character projection operators $P_{ir}^{C_{6v}^b}$ and $P_{ir}^{C_{6v}^t}$ of the bottom and top layers have three properties.

(i) $P_{ir}^{C_{6v}^b}$ and $P_{ir}^{C_{6v}^t}$ should be the same because of $\theta_t = 0°$, i.e.,

$$P_{ir}^{C_{6v}^b} = P_{ir}^{C_{6v}^t}. \tag{A14}$$

(ii) Because the characters of all operations in C_{6v} are real numbers and an arbitrary symmetry operation and its inverse

operation are inside the same class, the projection operators satisfy

$$\left[P_{ir}^{C_{6v}^b} \right]^\dagger = P_{ir}^{C_{6v}^b} = \left[P_{ir}^{C_{6v}^t} \right]^\dagger = P_{ir}^{C_{6v}^t}. \tag{A15}$$

(iii) C_{6v} is a subgroup of D_{6h}, and hence all symmetry operations in C_{6v} commute with the Hamiltonian H, i.e.,

$$\left[P_{ir}^{C_{6v}^b}, H \right] = \left[P_{ir}^{C_{6v}^t}, H \right] = 0. \tag{A16}$$

Using Eqs. (A14)–(A16), we write the hybridization matrix element $U_{ir,ir'}$ in untwisted BG as

$$U_{ir,ir'} = \left\langle \varphi_{ir}^b \left| H \right| \varphi_{ir'}^t \right\rangle = \left\langle \varphi_{ir}^b \left| P_{ir}^{C_{6v}^b} H \right| \varphi_{ir'}^t \right\rangle$$
$$= \left\langle \varphi_{ir}^b \left| H P_{ir}^{C_{6v}^b} \right| \varphi_{ir'}^t \right\rangle = \left\langle \varphi_{ir}^b \left| H P_{ir}^{C_{6v}^t} \right| \varphi_{ir'}^t \right\rangle$$
$$= \delta_{ir,ir'} U_{ir,ir'}. \tag{A17}$$

The constraint equation of $U_{ir,ir'}$ in Eq. (A17) endows hybridization rules for these states from the top and bottom layers, i.e., the hybridization selection rules in D_{6h} untwisted BG.

APPENDIX B: DETERMINATION OF IRREPS OF HYBRIDIZATION STATES

1. D_{6d} graphene quasicrystal

(i) For $A_1 + A_1 \Rightarrow A_1 + B_2$ hybridization with $\theta = 0$, the projection operators for A_1 and B_2 in D_{6d} take the form as

$$P_{A_1}^{D_{6d}} = \frac{1}{2} P_{A_1}^{C_{6v}} + \frac{1}{24} \left(\sum_{i=0}^{5} S_{12}^{2i+1} + \sum_{i=0}^{5} C_{2,i}' \right),$$
$$P_{B_2}^{D_{6d}} = \frac{1}{2} P_{A_1}^{C_{6v}} - \frac{1}{24} \left(\sum_{i=0}^{5} S_{12}^{2i+1} + \sum_{i=0}^{5} C_{2,i}' \right), \tag{B1}$$

with

$$S_{12}^{2i+1} \left| \phi_\pm^{A_1} \right\rangle = \pm \left| \phi_\pm^{A_1} \right\rangle,$$
$$C_{2,i}' \left| \phi_\pm^{A_1} \right\rangle = S_{12} \sigma_{d,i} \left| \phi_\pm^{A_1} \right\rangle = \pm \left| \phi_\pm^{A_1} \right\rangle. \tag{B2}$$

Using Eqs. (B1) and (B2), we have

$$P_{A_1}^{D_{6d}} \left| \phi_\pm^{A_1} \right\rangle = \frac{1}{2} \left| \phi_\pm^{A_1} \right\rangle \pm \frac{1}{2} \left| \phi_\pm \right\rangle,$$
$$P_{B_2}^{D_{6d}} \left| \phi_\pm^{A_1} \right\rangle = \frac{1}{2} \left| \phi_\pm^{A_1} \right\rangle \mp \frac{1}{2} \left| \phi_\pm \right\rangle. \tag{B3}$$

Equation (B3) indicates that $\left| \phi_+^{A_1} \right\rangle$ and $\left| \phi_-^{A_1} \right\rangle$ generated by $A_1 + A_1$ hybridization have irreps A_1 and B_2, respectively, in D_{6d} point group.

(ii) For $A_2 + A_2 \Rightarrow A_2 + B_1$ hybridization with $\theta = 0$, the projection operators for A_2 and B_1 in D_{6d} read as

$$P_{A_2}^{D_{6d}} = \frac{1}{2} P_{A_2}^{C_{6v}} + \frac{1}{24} \left(\sum_{i=0}^{5} S_{12}^{2i+1} - \sum_{i=0}^{5} C_{2,i}' \right),$$
$$P_{B_1}^{D_{6d}} = \frac{1}{2} P_{A_2}^{C_{6v}} - \frac{1}{24} \left(\sum_{i=0}^{5} S_{12}^{2i+1} - \sum_{i=0}^{5} C_{2,i}' \right), \tag{B4}$$

with

$$S_{12}^{2i+1} \left| \phi_\pm^{A_2} \right\rangle = \pm \left| \phi_\pm^{A_2} \right\rangle,$$
$$C_{2,i}' \left| \phi_\pm^{A_2} \right\rangle = S_{12} \sigma_{d,i} \left| \phi_\pm^{A_2} \right\rangle = \mp \left| \phi_\pm^{A_2} \right\rangle. \tag{B5}$$

Using Eqs. (B4) and (B5), we have

$$P_{A_2}^{D_{6d}}\big|\phi_{\pm}^{A_2}\big\rangle = \tfrac{1}{2}\big|\phi_{\pm}^{A_2}\big\rangle \pm \tfrac{1}{2}\big|\phi_{\pm}^{A_2}\big\rangle,$$
$$P_{B_1}^{D_{6d}}\big|\phi_{\pm}^{A_2}\big\rangle = \tfrac{1}{2}\big|\phi_{\pm}^{A_2}\big\rangle \mp \tfrac{1}{2}\big|\phi_{\pm}^{A_2}\big\rangle. \tag{B6}$$

Equation (B6) indicates that $\big|\phi_{+}^{A_2}\big\rangle$ and $\big|\phi_{-}^{A_2}\big\rangle$ generated by $A_2 + A_2$ hybridization have irreps A_2 and B_1, respectively, in D_{6d} point group.

(iii) For $E_1 + E_1 \Rightarrow E_1 + E_5$ hybridization with $\theta = \pm\frac{\pi}{3}$, the projection operators for E_1 and E_5 in D_{6d} read as

$$P_{E_1}^{D_{6d}} = \frac{1}{2}P_{E_1}^{C_{6v}} + \frac{2\sqrt{3}}{24}\big(S_{12} + S_{12}^{11} - S_{12}^5 - S_{12}^7\big),$$
$$P_{E_5}^{D_{6d}} = \frac{1}{2}P_{E_1}^{C_{6v}} - \frac{2\sqrt{3}}{24}\big(S_{12} + S_{12}^{11} - S_{12}^5 - S_{12}^7\big), \tag{B7}$$

with

$$\big(S_{12} + S_{12}^{11}\big)\big|\phi_{\pm}^{E_1}\big\rangle = \pm\sqrt{3}\big|\phi_{\pm}^{E_1}\big\rangle,$$
$$\big(S_{12}^5 + S_{12}^7\big)\big|\phi_{\pm}^{E_1}\big\rangle = \mp\sqrt{3}\big|\phi_{\pm}^{E_1}\big\rangle. \tag{B8}$$

Using Eqs. (B7) and (B8), we have

$$P_{E_1}^{D_{6d}}\big|\phi_{\pm}^{E_1}\big\rangle = \tfrac{1}{2}\big|\phi_{\pm}^{E_1}\big\rangle \pm \tfrac{1}{2}\big|\phi_{\pm}^{E_1}\big\rangle,$$
$$P_{E_5}^{D_{6d}}\big|\phi_{\pm}^{E_1}\big\rangle = \tfrac{1}{2}\big|\phi_{\pm}^{E_1}\big\rangle \mp \tfrac{1}{2}\big|\phi_{\pm}^{E_1}\big\rangle. \tag{B9}$$

Equation (B9) indicates that $\big|\phi_{+}^{E_1}\big\rangle$ and $\big|\phi_{-}^{E_1}\big\rangle$ generated by $E_1 + E_1$ hybridization have irreps E_1 and E_5, respectively, in D_{6d} point group.

(iv) For $E_2 + E_2 \Rightarrow E_2 + E_4$ hybridization with $\theta = \pm\frac{2\pi}{3}$, the projection operators for E_2 and E_4 in D_{6d} are expressed as

$$P_{E_2}^{D_{6d}} = \frac{1}{2}P_{E_2}^{C_{6v}} + \frac{2}{24}\sum_{i=0}^2 (-1)^i\big(S_{12}^{2i+1} + S_{12}^{11-2i}\big),$$
$$P_{E_4}^{D_{6d}} = \frac{1}{2}P_{E_2}^{C_{6v}} - \frac{2}{24}\sum_{i=0}^2 (-1)^i\big(S_{12}^{2i+1} + S_{12}^{11-2i}\big), \tag{B10}$$

with

$$\big(S_{12} + S_{12}^{11}\big)\big|\phi_{\pm}^{E_2}\big\rangle = \pm\big|\phi_{\pm}^{E_2}\big\rangle,$$
$$\big(S_{12}^3 + S_{12}^9\big)\big|\phi_{\pm}^{E_2}\big\rangle = \mp 2\big|\phi_{\pm}^{E_2}\big\rangle,$$
$$\big(S_{12}^5 + S_{12}^7\big)\big|\phi_{\pm}^{E_2}\big\rangle = \pm\big|\phi_{\pm}^{E_2}\big\rangle. \tag{B11}$$

Using Eqs. (B10) and (B11), we have

$$P_{E_2}^{D_{6d}}\big|\phi_{\pm}^{E_2}\big\rangle = \tfrac{1}{2}\big|\phi_{\pm}^{E_2}\big\rangle \pm \tfrac{1}{2}\big|\phi_{\pm}^{E_2}\big\rangle,$$
$$P_{E_4}^{D_{6d}}\big|\phi_{\pm}^{E_2}\big\rangle = \tfrac{1}{2}\big|\phi_{\pm}^{E_2}\big\rangle \mp \tfrac{1}{2}\big|\phi_{\pm}^{E_2}\big\rangle. \tag{B12}$$

Equation (B12) indicates that $\big|\phi_{+}^{E_2}\big\rangle$ and $\big|\phi_{-}^{E_2}\big\rangle$ generated by $E_2 + E_2$ hybridization have irreps E_2 and E_4, respectively, in D_{6d} point group.

(v) For $B_1 + B_2 \Rightarrow E_3 + E_3$ and $B_2 + B_1 \Rightarrow E_3 + E_3$ nonequivalent hybridizations in Eq. (8), the projection operator for E_3 in D_{6d} reads as

$$P_{E_3}^{D_{6d}} = \frac{2}{24}\big(2E - 2C_6 - 2C_6^5 + 2C_3 + 2C_3^2 - 2C_2\big). \tag{B13}$$

Equation (B13) indicates $P_{E_3}^{D_{6d}}$ is a combination of rotation operations, and these rotation operations are actually also

symmetry operations of C_{6v}. Thus, both $\big|\phi_{B_1}^{b/t}\big\rangle$ and $\big|\phi_{B_2}^{b/t}\big\rangle$ are eigenstates of $P_{E_3}^{D_{6d}}$, i.e.,

$$P_{E_3}^{D_{6d}}\big|\phi_{B_1}^{b/t}\big\rangle = \big|\phi_{B_1}^{b/t}\big\rangle,$$
$$P_{E_3}^{D_{6d}}\big|\phi_{B_2}^{b/t}\big\rangle = \big|\phi_{B_2}^{b/t}\big\rangle. \tag{B14}$$

Consequently, the states generated by $B_1 + B_2$ and $B_2 + B_1$ hybridizations must have ireep E_3 in D_{6d} point group.

2. D_6 twisted BG with $0° < \theta_t < 30°$

(i) For $A_1 + A_1 \Rightarrow A_1 + A_2$ hybridization, the projection operator for A_1 and A_2 in point group D_6 reads as

$$P_{A_1}^{D_6} = \frac{1}{12}\sum_{i=0}^5 C_6^i + \sum_{i=0}^2 C_{2,i}' + \sum_{i=0}^2 C_{2,i}'',$$
$$P_{A_2}^{D_6} = \frac{1}{12}\sum_{i=0}^5 C_6^i - \sum_{i=0}^2 C_{2,i}' - \sum_{i=0}^2 C_{2,i}'', \tag{B15}$$

where $C_{2,i}' = \sigma_h R(\frac{\theta_t}{2})\sigma_{v,i}^b R^\dagger(\frac{\theta_t}{2})$ and $C_{2,i}'' = \sigma_h R(\frac{\theta_t}{2})\sigma_{d,i}^b R^\dagger(\frac{\theta_t}{2})$. Using Eq. (B15) and

$$C_6^i\big|\phi_{\pm}^{A_1}\big\rangle = \big|\phi_{\pm}^{A_1}\big\rangle,$$
$$\sigma_{v,i}\big|\phi_{\pm}^{A_1}\big\rangle = \big|\phi_{\pm}^{A_1}\big\rangle, \quad \sigma_{d,i}\big|\phi_{\pm}^{A_1}\big\rangle = \big|\phi_{\pm}^{A_1}\big\rangle, \tag{B16}$$
$$C_{2,i}'\big|\phi_{\pm}^{A_1}\big\rangle = \pm\big|\phi_{\pm}^{A_1}\big\rangle, \quad C_{2,i}''\big|\phi_{\pm}^{A_1}\big\rangle = \pm\big|\phi_{\pm}^{A_1}\big\rangle,$$

where $\sigma_v R(\theta_t/2) = R^\dagger(\theta_t/2)\sigma_v$ is used, we have

$$P_{A_1}^{D_6}\big|\phi_{\pm}^{A_1}\big\rangle = \tfrac{1}{2}\big|\phi_{\pm}^{A_1}\big\rangle \pm \tfrac{1}{2}\big|\phi_{\pm}^{A_1}\big\rangle,$$
$$P_{A_2}^{D_6}\big|\phi_{\pm}^{A_1}\big\rangle = \tfrac{1}{2}\big|\phi_{\pm}^{A_1}\big\rangle \mp \tfrac{1}{2}\big|\phi_{\pm}^{A_1}\big\rangle. \tag{B17}$$

Equation (B17) indicates that $\big|\phi_{+}^{A_1}\big\rangle$ and $\big|\phi_{-}^{A_1}\big\rangle$ generated by $A_1 + A_1$ hybridization have irreps A_1 and A_2, respectively, in D_6 point group.

(ii) For $A_2 + A_2 \Rightarrow A_2 + A_1$ hybridization, using Eq. (B15) and

$$C_6^i\big|\phi_{\pm}^{A_2}\big\rangle = \big|\phi_{\pm}^{A_2}\big\rangle,$$
$$\sigma_{v,i}\big|\phi_{\pm}^{A_2}\big\rangle = -\big|\phi_{\pm}^{A_2}\big\rangle, \quad \sigma_{d,i}\big|\phi_{\pm}^{A_2}\big\rangle = -\big|\phi_{\pm}^{A_2}\big\rangle,$$
$$C_{2,i}'\big|\phi_{\pm}^{A_2}\big\rangle = \mp\big|\phi_{\pm}^{A_2}\big\rangle, \quad C_{2,i}''\big|\phi_{\pm}^{A_2}\big\rangle = \mp\big|\phi_{\pm}^{A_2}\big\rangle, \tag{B18}$$

we have

$$P_{A_2}^{D_6}\big|\phi_{\pm}^{A_2}\big\rangle = \tfrac{1}{2}\big|\phi_{\pm}^{A_2}\big\rangle \pm \tfrac{1}{2}\big|\phi_{\pm}^{A_2}\big\rangle,$$
$$P_{A_1}^{D_6}\big|\phi_{\pm}^{A_2}\big\rangle = \tfrac{1}{2}\big|\phi_{\pm}^{A_2}\big\rangle \mp \tfrac{1}{2}\big|\phi_{\pm}^{A_2}\big\rangle. \tag{B19}$$

Equation (B19) indicates that $\big|\phi_{+}^{A_2}\big\rangle$ and $\big|\phi_{-}^{A_2}\big\rangle$ generated by $A_2 + A_2$ hybridization have irreps A_2 and A_1, respectively, in D_6 point group.

(iii) For $B_1 + B_1 \Rightarrow B_1 + B_2$ hybridization, the projection operator for B_1 and B_2 in point group D_6 reads as

$$P_{B_1}^{D_6} = \frac{1}{12}\sum_{i=0}^5 (-1)^i C_6^i + \sum_{i=0}^2 C_{2,i}' - \sum_{i=0}^2 C_{2,i}'',$$
$$P_{B_2}^{D_6} = \frac{1}{12}\sum_{i=0}^5 (-1)^i C_6^i - \sum_{i=0}^2 C_{2,i}' + \sum_{i=0}^2 C_{2,i}''. \tag{B20}$$

Using Eq. (B20) and

$$C_6^i |\phi_\pm^{B_1}\rangle = (-1)^i |\phi_\pm^{B_1}\rangle,$$
$$\sigma_{v,i} |\phi_\pm^{B_1}\rangle = |\phi_\pm^{B_1}\rangle, \quad \sigma_{d,i} |\phi_\pm^{B_1}\rangle = -|\phi_\pm^{B_1}\rangle, \quad \text{(B21)}$$
$$C_{2,i}' |\phi_\pm^{B_1}\rangle = \pm |\phi_\pm^{B_1}\rangle, \quad C_{2,i}'' |\phi_\pm^{B_1}\rangle = \mp |\phi_\pm^{B_1}\rangle,$$

we have

$$P_{B_1}^{D_6} |\phi_\pm^{B_1}\rangle = \tfrac{1}{2} |\phi_\pm^{B_1}\rangle \pm \tfrac{1}{2} |\phi_\pm^{B_1}\rangle,$$
$$P_{B_2}^{D_6} |\phi_\pm^{B_1}\rangle = \tfrac{1}{2} |\phi_\pm^{B_1}\rangle \mp \tfrac{1}{2} |\phi_\pm^{B_1}\rangle. \quad \text{(B22)}$$

Equation (B22) indicates that $|\phi_+^{B_1}\rangle$ and $|\phi_-^{B_1}\rangle$ generated by $B_1 + B_1$ hybridization have irreps B_1 and B_2, respectively, in D_6 point group.

(iv) For $B_2 + B_2 \Rightarrow B_2 + B_1$ hybridization, using Eq. (B20) and

$$C_6^i |\phi_\pm^{B_2}\rangle = (-1)^i |\phi_\pm^{B_2}\rangle,$$
$$\sigma_{v,i} |\phi_\pm^{B_2}\rangle = -|\phi_\pm^{B_2}\rangle, \quad \sigma_{d,i} |\phi_\pm^{B_2}\rangle = |\phi_\pm^{B_2}\rangle,$$
$$C_{2,i}' |\phi_\pm^{B_2}\rangle = \mp |\phi_\pm^{B_2}\rangle, \quad C_{2,i}'' |\phi_\pm^{B_2}\rangle = \pm |\phi_\pm^{B_2}\rangle, \quad \text{(B23)}$$

we have

$$P_{B_2}^{D_6} |\phi_\pm^{B_2}\rangle = \tfrac{1}{2} |\phi_\pm^{B_2}\rangle \pm \tfrac{1}{2} |\phi_\pm^{B_2}\rangle,$$
$$P_{B_1}^{D_6} |\phi_\pm^{B_2}\rangle = \tfrac{1}{2} |\phi_\pm^{B_2}\rangle \mp \tfrac{1}{2} |\phi_\pm^{B_2}\rangle. \quad \text{(B24)}$$

Equation (B24) indicates that $|\phi_+^{B_2}\rangle$ and $|\phi_-^{B_2}\rangle$ generated by $B_2 + B_2$ hybridization have irreps B_2 and B_1, respectively, in D_6 point group.

(v) For equivalent hybridizations $E_i + E_i \Rightarrow E_i + E_i$ with $i = 1, 2$ in Eq. (11), because of $P_{E_i}^{C_{6v}^b} = P_{E_i}^{C_{6v}^t} = P_{E_i}^{D_6}$ in Eq. (A12), $|\phi_+^{E_i}\rangle$ and $|\phi_-^{E_i}\rangle$ generated by $E_i + E_i$ hybridization have irrep E_i in D_6 point group.

3. D_{6h} untwisted BG

(i) For $A_1 + A_1 \Rightarrow A_{1g} + A_{2u}$ hybridization, the relationships between the character projection operator for A_{1g} and A_{2u} in D_{6h} and A_1 in point group C_{6v} read as

$$P_{A_{1g}}^{D_{6h}} = \frac{1}{2} P_{A_1}^{C_{6v}} + \frac{1}{24} \left(\sum_{j=0}^{2} C_{2,j}' + \sum_{j=0}^{2} C_{2,j}'' \right)$$
$$+ \frac{1}{24} (i + S_3 + S_3^2 + S_6 + S_6^5 + \sigma_h),$$
$$P_{A_{2u}}^{D_{6h}} = \frac{1}{2} P_{A_1}^{C_{6v}} - \frac{1}{24} \left(\sum_{j=0}^{2} C_{2,j}' + \sum_{j=0}^{2} C_{2,j}'' \right)$$
$$- \frac{1}{24} (i + S_3 + S_3^2 + S_6 + S_6^5 + \sigma_h), \quad \text{(B25)}$$

where

$$C_{2,j}' = C_2 \sigma_{v,j} \sigma_h, \quad C_{2,j}'' = C_2 \sigma_{d,j} \sigma_h,$$
$$S_6^j = C_6^j \sigma_h, \quad i = S_6^3, \quad S_3 = S_6^2, \quad S_3^2 = S_6^4. \quad \text{(B26)}$$

Using Eqs. (B25) and (B26) and

$$P_{A_1}^{C_{6v}} |\phi_\pm^{A_1}\rangle = |\phi_\pm^{A_1}\rangle,$$
$$\sigma_h |\phi_\pm^{A_1}\rangle = \pm |\phi_\pm^{A_1}\rangle, \quad C_6^i |\phi_\pm^{A_1}\rangle = |\phi_\pm^{A_1}\rangle,$$
$$\sigma_{v,i} |\phi_\pm^{A_1}\rangle = |\phi_\pm^{A_1}\rangle, \quad \sigma_{d,i} |\phi_\pm^{A_1}\rangle = |\phi_\pm^{A_1}\rangle, \quad \text{(B27)}$$

we have

$$P_{A_{1g}}^{D_{6h}} |\phi_\pm^{A_1}\rangle = \tfrac{1}{2} |\phi_\pm^{A_1}\rangle \pm \tfrac{1}{2} |\phi_\pm^{A_1}\rangle,$$
$$P_{A_{2u}}^{D_{6h}} |\phi_\pm^{A_1}\rangle = \tfrac{1}{2} |\phi_\pm^{A_1}\rangle \mp \tfrac{1}{2} |\phi_\pm^{A_1}\rangle. \quad \text{(B28)}$$

Equation (B28) indicates that $|\phi_+^{A_1}\rangle$ and $|\phi_-^{A_1}\rangle$ generated by $A_1 + A_1$ hybridization have irreps A_{1g} and A_{2u}, respectively, in D_{6h} point group.

(ii) For $A_2 + A_2 \Rightarrow A_{2g} + A_{1u}$ hybridization, the relationships between the character projection operator for A_{2g} and A_{1u} in D_{6h} and A_2 in point group C_{6v} read as

$$P_{A_{2g}}^{D_{6h}} = \frac{1}{2} P_{A_2}^{C_{6v}} + \frac{1}{24} \left(-\sum_{j=0}^{2} C_{2,j}' - \sum_{j=0}^{2} C_{2,j}'' \right)$$
$$+ \frac{1}{24} (i + S_3 + S_3^2 + S_6 + S_6^5 + \sigma_h),$$
$$P_{A_{1u}}^{D_{6h}} = \frac{1}{2} P_{A_2}^{C_{6v}} - \frac{1}{24} \left(-\sum_{j=0}^{2} C_{2,j}' - \sum_{j=0}^{2} C_{2,j}'' \right)$$
$$- \frac{1}{24} (i + S_3 + S_3^2 + S_6 + S_6^5 + \sigma_h). \quad \text{(B29)}$$

Using Eqs. (B26) and (B29) and

$$P_{A_2}^{C_{6v}} |\phi_\pm^{A_2}\rangle = |\phi_\pm^{A_2}\rangle,$$
$$\sigma_h |\phi_\pm^{A_2}\rangle = \pm |\phi_\pm^{A_2}\rangle, \quad C_6^i |\phi_\pm^{A_2}\rangle = |\phi_\pm^{A_2}\rangle,$$
$$\sigma_{v,i} |\phi_\pm^{A_2}\rangle = -|\phi_\pm^{A_2}\rangle, \quad \sigma_{d,i} |\phi_\pm^{A_2}\rangle = -|\phi_\pm^{A_2}\rangle, \quad \text{(B30)}$$

we have

$$P_{A_{2g}}^{D_{6h}} |\phi_\pm^{A_2}\rangle = \tfrac{1}{2} |\phi_\pm^{A_2}\rangle \pm \tfrac{1}{2} |\phi_\pm^{A_2}\rangle,$$
$$P_{A_{1u}}^{D_{6h}} |\phi_\pm^{A_2}\rangle = \tfrac{1}{2} |\phi_\pm^{A_2}\rangle \mp \tfrac{1}{2} |\phi_\pm^{A_2}\rangle. \quad \text{(B31)}$$

Equation (B31) indicates that $|\phi_+^{A_2}\rangle$ and $|\phi_-^{A_2}\rangle$ generated by $A_2 + A_2$ hybridization have irreps A_{2g} and A_{1u}, respectively, in D_{6h} point group.

(iii) For $B_1 + B_1 \Rightarrow B_{1u} + B_{2g}$ hybridization, the relationships between the character projection operator for B_{2g} and B_{1u} in D_{6h} and B_1 in point group C_{6v} read as

$$P_{B_{1u}}^{D_{6h}} = \frac{1}{2} P_{B_1}^{C_{6v}} - \frac{1}{24} \left(-\sum_{j=0}^{2} C_{2,j}' + \sum_{j=0}^{2} C_{2,j}'' \right)$$
$$- \frac{1}{24} (i - S_3 - S_3^2 + S_6 + S_6^5 - \sigma_h),$$
$$P_{B_{2g}}^{D_{6h}} = \frac{1}{2} P_{B_1}^{C_{6v}} + \frac{1}{24} \left(-\sum_{j=0}^{2} C_{2,j}' + \sum_{j=0}^{2} C_{2,j}'' \right)$$
$$+ \frac{1}{24} (i - S_3 - S_3^2 + S_6 + S_6^5 - \sigma_h). \quad \text{(B32)}$$

Using Eqs. (B26) and (B32) and

$$P_{B_1}^{C_{6v}}|\phi_{\pm}^{B_1}\rangle = |\phi_{\pm}^{B_1}\rangle,$$
$$\sigma_h|\phi_{\pm}^{B_1}\rangle = \pm|\phi_{\pm}^{B_1}\rangle, \quad C_6^i|\phi_{\pm}^{B_1}\rangle = (-1)^i|\phi_{\pm}^{B_1}\rangle,$$
$$\sigma_{v,i}|\phi_{\pm}^{B_1}\rangle = |\phi_{\pm}^{B_1}\rangle, \quad \sigma_{d,i}|\phi_{\pm}^{B_1}\rangle = -|\phi_{\pm}^{B_1}\rangle, \tag{B33}$$

we have

$$P_{B_{1u}}^{D_{6h}}|\phi_{\pm}^{B_1}\rangle = \tfrac{1}{2}|\phi_{\pm}^{B_1}\rangle \pm \tfrac{1}{2}|\phi_{\pm}^{B_1}\rangle,$$
$$P_{B_{2g}}^{D_{6h}}|\phi_{\pm}^{B_1}\rangle = \tfrac{1}{2}|\phi_{\pm}^{B_1}\rangle \mp \tfrac{1}{2}|\phi_{\pm}^{B_1}\rangle. \tag{B34}$$

Equation (B34) indicates that $|\phi_{+}^{B_1}\rangle$ and $|\phi_{-}^{B_1}\rangle$ generated by $B_1 + B_1$ hybridization have irreps B_{1u} and B_{2g}, respectively, in D_{6h} point group.

(iv) For $B_2 + B_2 \Rightarrow B_{2u} + B_{1g}$ hybridization, the relationships between the character projection operator for B_{1g} and B_{2u} in D_{6h} and B_2 in point group C_{6v} read as

$$P_{B_{2u}}^{D_{6h}} = \frac{1}{2}P_{B_2}^{C_{6v}} - \frac{1}{24}\left(\sum_{j=0}^{2}C_{2,j}' - \sum_{j=0}^{2}C_{2,j}''\right)$$
$$\qquad - \frac{1}{24}\left(i - S_3 - S_3^2 + S_6 + S_6^5 - \sigma_h\right),$$
$$P_{B_{1g}}^{D_{6h}} = \frac{1}{2}P_{B_2}^{C_{6v}} + \frac{1}{24}\left(\sum_{j=0}^{2}C_{2,j}' - \sum_{j=0}^{2}C_{2,j}''\right)$$
$$\qquad + \frac{1}{24}\left(i - S_3 - S_3^2 + S_6 + S_6^5 - \sigma_h\right). \tag{B35}$$

Using Eqs. (B26) and (B35) and

$$P_{B_1}^{C_{6v}}|\phi_{\pm}^{B_2}\rangle = |\phi_{\pm}^{B_2}\rangle,$$
$$\sigma_h|\phi_{\pm}^{B_2}\rangle = \pm|\phi_{\pm}^{B_2}\rangle, \quad C_6^i|\phi_{\pm}^{B_2}\rangle = (-1)^i|\phi_{\pm}^{B_2}\rangle,$$
$$\sigma_{v,i}|\phi_{\pm}^{B_2}\rangle = -|\phi_{\pm}^{B_2}\rangle, \quad \sigma_{d,i}|\phi_{\pm}^{B_2}\rangle = |\phi_{\pm}^{B_2}\rangle, \tag{B36}$$

we have

$$P_{B_{2u}}^{D_{6h}}|\phi_{\pm}^{B_2}\rangle = \tfrac{1}{2}|\phi_{\pm}^{B_2}\rangle \pm \tfrac{1}{2}|\phi_{\pm}^{B_2}\rangle,$$
$$P_{B_{1g}}^{D_{6h}}|\phi_{\pm}^{B_2}\rangle = \tfrac{1}{2}|\phi_{\pm}^{B_2}\rangle \mp \tfrac{1}{2}|\phi_{\pm}^{B_2}\rangle. \tag{B37}$$

Equation (B37) indicates that $|\phi_{+}^{B_2}\rangle$ and $|\phi_{-}^{B_2}\rangle$ generated by $B_2 + B_2$ hybridization have irreps B_{2u} and B_{1g}, respectively, in D_{6h} point group.

(v) For $E_1 + E_1 \Rightarrow E_{1u} + E_{1g}$ hybridization, the relationships between the character projection operator for E_{1u} and E_{1g} in D_{6h} and E_1 in point group C_{6v} read as

$$P_{E_{1u}}^{D_{6h}} = \tfrac{1}{2}P_{E_1}^{C_{6v}} - \tfrac{2}{24}\left(2i + S_3 + S_3^2 - S_6 - S_6^5 - 2\sigma_h\right),$$
$$P_{E_{1g}}^{D_{6h}} = \tfrac{1}{2}P_{E_1}^{C_{6v}} + \tfrac{2}{24}\left(2i + S_3 + S_3^2 - S_6 - S_6^5 - 2\sigma_h\right). \tag{B38}$$

In C_{6v} monolayer a 2D E_1 state is the eigenstate of C_6 with the corresponding eigenvalue $e^{\pm i\pi/3}$, i.e., $C_6|\phi_{\pm}^{E_1}\rangle = e^{\pm i\pi/3}|\phi_{\pm}^{E_1}\rangle$. Using Eqs. (B26) and (B38) and

$$P_{E_1}^{C_{6v}}|\phi_{\pm}^{E_1}\rangle = |\phi_{\pm}^{E_1}\rangle,$$
$$\sigma_h|\phi_{\pm}^{E_1}\rangle = \pm|\phi_{\pm}^{E_1}\rangle, \tag{B39}$$
$$C_6^j|\phi_{\pm}^{E_1}\rangle = (e^{\pm i\pi/3})^j|\phi_{\pm}^{E_1}\rangle,$$

we have

$$P_{E_{1u}}^{D_{6h}}|\phi_{\pm}^{E_1}\rangle = \tfrac{1}{2}|\phi_{\pm}^{E_1}\rangle \pm \tfrac{1}{2}|\phi_{\pm}^{E_1}\rangle,$$
$$P_{E_{1g}}^{D_{6h}}|\phi_{\pm}^{E_1}\rangle = \tfrac{1}{2}|\phi_{\pm}^{E_1}\rangle \mp \tfrac{1}{2}|\phi_{\pm}^{E_1}\rangle. \tag{B40}$$

Equation (B40) indicates that $|\phi_{+}^{E_1}\rangle$ and $|\phi_{-}^{E_1}\rangle$ generated by $E_1 + E_1$ hybridization have irreps E_{1u} and E_{1g}, respectively, in D_{6h} point group.

(vi) For $E_2 + E_2 \Rightarrow E_{2g} + E_{2u}$ hybridization, the relationships between the character projection operator for E_{2g} and E_{2u} in D_{6h} and E_2 in point group C_{6v} read as

$$P_{E_{2g}}^{D_{6h}} = \tfrac{1}{2}P_{E_2}^{C_{6v}} + \tfrac{2}{24}\left(2i - S_3 - S_3^2 - S_6 - S_6^5 + 2\sigma_h\right),$$
$$P_{E_{2u}}^{D_{6h}} = \tfrac{1}{2}P_{E_2}^{C_{6v}} - \tfrac{2}{24}\left(2i - S_3 - S_3^2 - S_6 - S_6^5 + 2\sigma_h\right). \tag{B41}$$

In C_{6v} monolayer a 2D E_2 state is the eigenstate of C_6 with the corresponding eigenvalue $e^{\pm i2\pi/3}$, i.e., $C_6|\phi_{\pm}^{E_2}\rangle = e^{\pm i2\pi/3}|\phi_{\pm}^{E_2}\rangle$. Using Eqs. (B26) and (B41) and

$$P_{E_2}^{C_{6v}}|\phi_{\pm}^{E_2}\rangle = |\phi_{\pm}^{E_2}\rangle,$$
$$\sigma_h|\phi_{\pm}^{E_2}\rangle = \pm|\phi_{\pm}^{E_2}\rangle, \tag{B42}$$
$$C_6^j|\phi_{\pm}^{E_2}\rangle = (e^{\pm i2\pi/3})^j|\phi_{\pm}^{E_2}\rangle,$$

we have

$$P_{E_{2g}}^{D_{6h}}|\phi_{\pm}^{E_2}\rangle = \tfrac{1}{2}|\phi_{\pm}^{E_2}\rangle \pm \tfrac{1}{2}|\phi_{\pm}^{E_2}\rangle,$$
$$P_{E_{2u}}^{D_{6h}}|\phi_{\pm}^{E_2}\rangle = \tfrac{1}{2}|\phi_{\pm}^{E_2}\rangle \mp \tfrac{1}{2}|\phi_{\pm}^{E_2}\rangle. \tag{B43}$$

Equation (B43) indicates that $|\phi_{+}^{E_2}\rangle$ and $|\phi_{-}^{E_2}\rangle$ generated by $E_2 + E_2$ hybridization have irreps E_{2g} and E_{2u}, respectively, in D_{6h} point group.

APPENDIX C: p_z-ORBITAL TB MODEL

In the p_z-orbital TB model, the hopping energy between sites i and j is determined by [49]

$$t(\mathbf{r}_{ij}) = n^2 V_{pp\sigma}(|\mathbf{r}_{ij}|) + (1 - n^2)V_{pp\pi}(|\mathbf{r}_{ij}|), \tag{C1}$$

where n is the direction cosine of relative position vector $\mathbf{r}_{ij}$ with respect to the z axis. The Slater-Koster parameters $V_{pp\sigma}$ and $V_{pp\pi}$ read as

$$V_{pp\pi}(|\mathbf{r}_{ij}|) = -\gamma_0 e^{2.218(b-|\mathbf{r}_{ij}|)}F_c(|\mathbf{r}_{ij}|),$$
$$V_{pp\sigma}(|\mathbf{r}_{ij}|) = \gamma_1 e^{2.218(h-|\mathbf{r}_{ij}|)}F_c(|\mathbf{r}_{ij}|), \tag{C2}$$

where γ_0 and γ_1 are 2.7 and 0.48 eV, respectively, $b = 1.42$ Å is the nearest intralayer carbon-carbon distance, and F_c is a smooth function

$$F_c(r) = (1 + e^{(r-0.265)/5})^{-1}. \tag{C3}$$

In our calculations, a large cutoff carbon-carbon distance for the hopping energy is adopted up to 5 Å. In this p_z-orbital-based TB model, the van der Waals interaction has been included in the interlayer hopping. The p_z-orbital TB model has been widely used to predict the electronic structures and exotic states [17,27,33,50–56] in good accordance with experimental results [17,51–53] in twisted BG systems.

TABLE VII. The 10 interlayer hopping parameters in units of eV [57].

λ_0	ξ_0	κ_0	λ_3	ξ_3	x_3	λ_6	ξ_6	x_6	κ_6
0.310	1.750	1.990	−0.068	3.286	0.500	−0.008	2.727	1.217	1.562

APPENDIX D: WANNIER-ORBITAL TB MODEL

The Wannier-orbital TB model in twisted BG is proposed by Fang and Kaxiras [57]. Compared with the p_z-orbital TB model, the Wannier-orbital TB model can reproduce the electronic structure of DFT calculations on twisted BG accurately even in higher-energy region without increasing the computational cost. In this model, the intralayer hopping energies up to the eighth-nearest neighbors, which are −2.8922, 0.2425, −0.2656, 0.0235, 0.0524, −0.0209, −0.0148, and −0.0211 eV from the first- to eighth-nearest neighbors, respectively, are used to describe the Hamiltonian of graphene monolayer. The interlayer hopping in a functional form depending on both distance and orientation reads as [57]

$$t(\mathbf{r}) = V_0(r) + V_3(r)[\cos(3\theta_{12}) + \cos(3\theta_{21})]$$
$$+ V_6(r)[\cos(6\theta_{12}) + \cos(6\theta_{21})], \quad \text{(D1)}$$

where $\mathbf{r}$ is the in-plane part of the vector connecting two sites, $r = |\mathbf{r}|$ describes the projected distance between two Wannier functions, and θ_{12} and θ_{21} are the angles between the projected interlayer bond and the in-plane nearest-neighbor bonds, describing the relative orientation of the two Wannier functions. The three radial functions in Eq. (D1) depend on 10 hopping parameters ($\bar{r} = r/a$) as follows:

$$V_0(r) = \lambda_0 e^{-\xi_0 \bar{r}^2} \cos(\kappa_0 \bar{r}),$$
$$V_3(r) = \lambda_3 \bar{r}^2 e^{-\xi_3 (\bar{r} - x_3)^2}, \quad \text{(D2)}$$
$$V_6(r) = \lambda_6 e^{-\xi_6 (\bar{r} - x_6)^2} \sin(\kappa_6 \bar{r}),$$

where related parameters are listed in Table VII.

APPENDIX E: DFT CALCULATIONS

The density functional theory (DFT) calculations are implemented in SIESTA code [58]. First, graphene monolayer quantum dot, inside a 30 Å × 30 Å × 15 Å box avoiding the interaction between adjacent images, is relaxed until the maximal force less than 0.04 eV/Å under the GGA-PBE functional and double-zeta polarization (DZP) basis sets. Second, we perform the self-consistent calculations on the size-2 untwisted and twisted BG quantum dots inside a 30 Å × 30 Å × 30 Å box, where two relaxed monolayers are overlaid in z direction with the same twist angle θ_t and the inter-layer distance $h = 3.35$ Å as the value used in p_z-orbital and Wannier-orbital TB models. The optB88-vdW functional and SZ bases are adopted during the self-consistent calculation. Note that for all DFT calculations, the edge carbon atoms are saturated by hydrogen atoms. Finally, the Hamiltonian (H) and overlap (S) matrices are obtained with the help of SISL tool [59]. Because the energy states inside low-energy area have mainly the p_z-orbital character, the components with p_z orbital involved are picked up. The eigenstates are obtained by solving the generalized eigenequation $H\phi = \varepsilon S\phi$. After separating the eigenstates of each layer according to the irrep of C_{6v} point group and the rotation C_6, we obtain the interlayer hybridization and overlap matrix elements.

APPENDIX F: TIGHT-BINDING PROPAGATION METHOD FOR OPTICAL CONDUCTIVITY

The interband optical conductivity (i.e., not including the Drude part at $\omega = 0$) is calculated by using the Kubo formula realized in TB propagation method [60], where the real part of the optical conductivity matrix $\sigma = \sigma_{xx}$ at temperature T reads as

$$\text{Re}\,\sigma_{xx}(\omega) = \lim_{\epsilon \to 0^+} \frac{e^{-\hbar\omega/k_B T} - 1}{\hbar\omega A} \int_0^\infty e^{-\epsilon\tau} \sin\omega\tau$$
$$\times 2\,\text{Im}\langle j_x\phi_2(\tau)|j_x\phi_1(\tau)\rangle d\tau. \quad \text{(F1)}$$

In Eq. (F1), A is the area of unit cell, and the wave functions read as

$$|\phi_1(\tau)\rangle = e^{-iH\tau/\hbar}[1 - f(H)]|\phi_0\rangle,$$
$$|\phi_2(\tau)\rangle = e^{-iH\tau/\hbar} f(H)|\phi_0\rangle, \quad \text{(F2)}$$

where $|\phi_0\rangle$ is the normalized initial state as a random superposition of p_z orbitals at all sites, and $f(H) = 1/(e^{(H-\mu)/k_B T} + 1)$ is the Fermi-Dirac distribution operator with μ as the chemical potential. j_x is the current operator along the x direction, for a TB model, which reads as

$$j_x = -\frac{ie}{\hbar} \sum_{ij} t_{ij}(x_j - x_i) C_i^\dagger C_j, \quad \text{(F3)}$$

where $x_j - x_i$ is the x component of the relative position vector from site i to site j.

[1] Y. Cao, V. Fatemi, S. Fang, K. Watanabe, T. Taniguchi, E. Kaxiras, and P. Jarillo-Herrero, Nature (London) **556**, 43 (2018).

[2] H. C. Po, L. Zou, A. Vishwanath, and T. Senthil, Phys. Rev. X **8**, 031089 (2018).

[3] M. Yankowitz, S. Chen, H. Polshyn, Y. Zhang, K. Watanabe, T. Taniguchi, D. Graf, A. F. Young, and C. R. Dean, Science **363**, 1059 (2019).

[4] C. Xu and L. Balents, Phys. Rev. Lett. **121**, 087001 (2018).

[5] J. M. B. Lopes dos Santos, N. M. R. Peres, and A. H. Castro Neto, Phys. Rev. Lett. **99**, 256802 (2007).

[6] E. Suárez Morell, J. D. Correa, P. Vargas, M. Pacheco, and Z. Barticevic, Phys. Rev. B **82**, 121407(R) (2010).

[7] R. Bistritzer and A. H. MacDonald, Proc. Natl. Acad. Sci. USA **108**, 12233 (2011).

[8] Y. Cao, V. Fatemi, A. Demir, S. Fang, S. L. Tomarken, J. Y. Luo, J. D. Sanchez-Yamagishi, K. Watanabe, T. Taniguchi, E. Kaxiras, R. C. Ashoori, and P. Jarillo-Herrero, Nature (London) **556**, 80 (2018).

[9] J. Kang and O. Vafek, Phys. Rev. Lett. **122**, 246401 (2019).

[10] B. A. Bernevig, B. Lian, A. Cowsik, F. Xie, N. Regnault, and Z.-D. Song, Phys. Rev. B **103**, 205415 (2021).

[11] B. Padhi, C. Setty, and P. W. Phillips, Nano Lett. **18**, 6175 (2018).

[12] F. Wu, A. H. MacDonald, and I. Martin, Phys. Rev. Lett. **121**, 257001 (2018).

[13] F. Wu and S. Das Sarma, Phys. Rev. B **99**, 220507(R) (2019).

[14] E. Codecido, Q. Wang, R. Koester, S. Che, H. Tian, R. Lv, S. Tran, K. Watanabe, T. Taniguchi, F. Zhang, M. Bockrath, and C. N. Lau, Sci. Adv. **5**, eaaw9770 (2019).

[15] J. Liu and X. Dai, Phys. Rev. B **103**, 035427 (2021).

[16] M. Koshino, N. F. Q. Yuan, T. Koretsune, M. Ochi, K. Kuroki, and L. Fu, Phys. Rev. X **8**, 031087 (2018).

[17] S. J. Ahn, P. Moon, T.-H. Kim, H.-W. Kim, H.-C. Shin, E. H. Kim, H. W. Cha, S.-J. Kahng, P. Kim, M. Koshino, Y.-W. Son, C.-W. Yang, and J. R. Ahn, Science **361**, 782 (2018).

[18] W. Yao, E. Wang, C. Bao, Y. Zhang, K. Zhang, K. Bao, C. K. Chan, C. Chen, J. Avila, M. C. Asensio, J. Zhu, and S. Zhou, Proc. Natl. Acad. Sci. USA **115**, 6928 (2018).

[19] F. C. Bocquet, Y.-R. Lin, M. Franke, N. Samiseresht, S. Parhizkar, S. Soubatch, T.-L. Lee, C. Kumpf, and F. S. Tautz, Phys. Rev. Lett. **125**, 106102 (2020).

[20] Y. Takesaki, K. Kawahara, H. Hibino, S. Okada, M. Tsuji, and H. Ago, Chem. Mater. **28**, 4583 (2016).

[21] C. Yan, D.-L. Ma, J.-B. Qiao, H.-Y. Zhong, L. Yang, S.-Y. Li, Z.-Q. Fu, Y. Zhang, and L. He, 2D Mater. **6**, 045041 (2019).

[22] T. Suzuki, T. Iimori, S. J. Ahn, Y. Zhao, M. Watanabe, J. Xu, M. Fujisawa, T. Kanai, N. Ishii, J. Itatani, K. Suwa, H. Fukidome, S. Tanaka, J. R. Ahn, K. Okazaki, S. Shin, F. Komori, and I. Matsuda, ACS Nano **13**, 11981 (2019).

[23] S. Pezzini, V. Mišeikis, G. Piccinini, S. Forti, S. Pace, R. Engelke, F. Rossella, K. Watanabe, T. Taniguchi, P. Kim, and C. Coletti, Nano Lett. **20**, 3313 (2020).

[24] B. Deng, B. Wang, N. Li, R. Li, Y. Wang, J. Tang, Q. Fu, Z. Tian, P. Gao, J. Xue, and H. Peng, ACS Nano **14**, 1656 (2020).

[25] J. Liu, Z. Wang, D. Ling, D. Wei, W. Lv, X. Kang, F. Qi, S. Ding, X. Hao, P. Li, and Y. Chen, 2D Mater. **8**, 021002 (2021).

[26] M. J. Park, H. S. Kim, and S. B. Lee, Phys. Rev. B **99**, 245401 (2019).

[27] P. Moon, M. Koshino, and Y.-W. Son, Phys. Rev. B **99**, 165430 (2019).

[28] E. Koren and U. Duerig, Phys. Rev. B **93**, 201404(R) (2016).

[29] J. A. Crosse and P. Moon, Phys. Rev. B **103**, 045408 (2021).

[30] S. Spurrier and N. R. Cooper, Phys. Rev. B **100**, 081405(R) (2019).

[31] G. Yu, Z. Wu, Z. Zhan, M. I. Katsnelson, and S. Yuan, npj Comput. Mater. **5**, 122 (2019).

[32] G. Yu, M. I. Katsnelson, and S. Yuan, Phys. Rev. B **102**, 045113 (2020).

[33] G. Yu, Z. Wu, Z. Zhan, M. I. Katsnelson, and S. Yuan, Phys. Rev. B **102**, 115123 (2020).

[34] Z. Li and Z. F. Wang, Chin. Phys. B **29**, 107101 (2020).

[35] Y.-B. Liu, Y. Zhang, W.-Q. Chen, and F. Yang, arXiv:2106.08542.

[36] D. Shechtman, I. Blech, D. Gratias, and J. W. Cahn, Phys. Rev. Lett. **53**, 1951 (1984).

[37] D. Levine and P. J. Steinhardt, Phys. Rev. Lett. **53**, 2477 (1984).

[38] J. Hass, F. Varchon, J. E. Millán-Otoya, M. Sprinkle, N. Sharma, W. A. de Heer, C. Berger, P. N. First, L. Magaud, and E. H. Conrad, Phys. Rev. Lett. **100**, 125504 (2008).

[39] M. Sprinkle, D. Siegel, Y. Hu, J. Hicks, A. Tejeda, A. Taleb-Ibrahimi, P. Le Fèvre, F. Bertran, S. Vizzini, H. Enriquez, S. Chiang, P. Soukiassian, C. Berger, W. A. de Heer, A. Lanzara, and E. H. Conrad, Phys. Rev. Lett. **103**, 226803 (2009).

[40] E. J. Mele, Phys. Rev. B **81**, 161405(R) (2010).

[41] S. Shallcross, S. Sharma, E. Kandelaki, and O. A. Pankratov, Phys. Rev. B **81**, 165105 (2010).

[42] S. Shallcross, S. Sharma, and O. Pankratov, Phys. Rev. B **87**, 245403 (2013).

[43] D. Weckbecker, S. Shallcross, M. Fleischmann, N. Ray, S. Sharma, and O. Pankratov, Phys. Rev. B **93**, 035452 (2016).

[44] M. Koshino, New J. Phys. **17**, 015014 (2015).

[45] Y. Wang, G. Yu, M. Rösner, M. I. Katsnelson, H.-Q. Lin, and S. Yuan, arXiv:2110.01323.

[46] K. A. Ritter and J. W. Lyding, Nat. Mater. **8**, 235 (2009).

[47] P. Ruffieux, S. Wang, B. Yang, C. Sánchez-Sánchez, J. Liu, T. Dienel, L. Talirz, P. Shinde, C. A. Pignedoli, D. Passerone, T. Dumslaff, X. Feng, K. Müllen, and R. Fasel, Nature (London) **531**, 489 (2016).

[48] G. D. Nguyen, H.-Z. Tsai, A. A. Omrani, T. Marangoni, M. Wu, D. J. Rizzo, G. F. Rodgers, R. R. Cloke, R. A. Durr, Y. Sakai, F. Liou, A. S. Aikawa, J. R. Chelikowsky, S. G. Louie, F. R. Fischer, and M. F. Crommie, Nat. Nanotechnol. **12**, 1077 (2017).

[49] J. C. Slater and G. F. Koster, Phys. Rev. **94**, 1498 (1954).

[50] G. Trambly de Laissardière, D. Mayou, and L. Magaud, Phys. Rev. B **86**, 125413 (2012).

[51] L. Huder, A. Artaud, T. Le Quang, G. T. de Laissardière, A. G. M. Jansen, G. Lapertot, C. Chapelier, and V. T. Renard, Phys. Rev. Lett. **120**, 156405 (2018).

[52] H. Shi, Z. Zhan, Z. Qi, K. Huang, E. v. Veen, J. Á. Silva-Guillén, R. Zhang, P. Li, K. Xie, H. Ji, M. I. Katsnelson, S. Yuan, S. Qin, and Z. Zhang, Nat. Commun. **11**, 371 (2020).

[53] A. Kerelsky, L. J. McGilly, D. M. Kennes, L. Xian, M. Yankowitz, S. Chen, K. Watanabe, T. Taniguchi, J. Hone, C. Dean, A. Rubio, A. N. Pasupathy, Nature (London) **572**, 95 (2019).

[54] X. Liang, Z. A. H. Goodwin, V. Vitale, F. Corsetti, A. A. Mostofi, and J. Lischner, Phys. Rev. B **102**, 155146 (2020).

[55] V. N. Do, H. A. Le, and D. Bercioux, Phys. Rev. B **99**, 165127 (2019).

[56] Z.-H. Wang, F. Xu, L. Li, R. Lü, B. Wang, and W.-Q. Chen, Phys. Rev. B **100**, 094531 (2019).

[57] S. Fang and E. Kaxiras, Phys. Rev. B **93**, 235153 (2016).

[58] J. M. Soler, E. Artacho, J. D. Gale, A. García, J. Junquera, P. Ordejón, and D. Sánchez-Portal, J. Phys.: Condens. Matter **14**, 2745 (2002).

[59] N. Papior, SISL: v0.11.0 (2021), doi: 10.5281/zenodo.597181.

[60] S. Yuan, H. De Raedt, and M. I. Katsnelson, Phys. Rev. B **82**, 115448 (2010).